Acta Materialia 263 (2024) 119462

Contents lists available at ScienceDirect

Acta Materialia

journal homepage: www.elsevier.com/locate/actamat

Full length article

In situ characterization of thermomechanically loaded solution strengthened, nanocrystalline nickel alloys

Thomas R. Koenig [a], Hongyu Wang [b], Yong Zhu [b], Ankit Gupta [c,d], Garritt J. Tucker [c,d], Gregory B. Thompson [a,*]

[a] University of Alabama, Department of Metallurgical & Materials Engineering, Tuscaloosa, AL 35401, United States
[b] North Carolina State University, Department of Mechanical and Aerospace Engineering, Raleigh, NC 27695, United States
[c] Colorado School of Mines, Department of Mechanical Engineering, CO, United States
[d] Baylor University, Department of Physics, Waco, TX 76798, United States

ARTICLE INFO

Keywords:
MEMS
In situ
TEM
Fracture
Nanocrystalline

ABSTRACT

Nanocrystalline (NC) Ni-40Cu and Ni-40Cu-0.6P (at.%) alloys were mechanically loaded in tension at ambient (23 °C) and elevated (150 °C) temperatures with the deformed nanostructure captured by *in situ* transmission electron microscopy coupled with digital image correlation for data mining high strain regions prior to catastrophic failure. The addition of the P provided grain boundary partitioning that stabilized the NC structure under both loading cases, which was not found to be the case for the binary alloy. While mechanical strength softening was observed in each of the alloys upon thermomechanical loading, the retention of strength was substantially higher in the ternary alloy than its binary counterpart. Digital image correlation was found to be a useful means for image mining to identify different regions where failure mechanisms were initiated. Intergranular failure was observed as the dominant failure mechanism in all specimens with the binary alloy revealing a coarser fracture profile as compared to a finer fracture profile in the ternary alloy. Atomistic simulations are used to understand P solute strengthening of the grain boundaries against this fracture failure mode.

1. Introduction

Over the last 30 years, nanocrystalline (NC) alloys have been modeled [1–10], fabricated [11–16], and characterized [11–19] to reap the benefits of the Hall-Petch relationship [20,21]. Significant efforts have been made to study the mechanisms governing the strength gained by reducing the grain size (GS) of a material to retain that strength throughout deformation. While NC alloys exhibit exceptional strength from their nanometer sized grains, these grains are inherently unstable because of the high radius of curvature described by the Gibbs-Thomson effect [22]. The application of thermal [23–25] and/or mechanical [26–30] stimuli results in significant grain coarsening to reduce this radius of curvature resulting in an associated reduction in strength. The mitigation of such detrimental grain growth has been approached from two primary concepts – kinetically pinning the grain boundaries (GBs) [31,32] and/or reducing the thermodynamic driving force for grain growth, *i.e.*, making the Gibbsian excess free energy trend towards zero [1,15]. These approaches have each manifested themselves in materials which are reported to be NC stabilized. In the Cu-Ta alloy system, nanoscale Ta precipitates out of solution pinning the boundaries resulting in excellent stability up to temperatures of 1000 °C [3,33]. Even under mechanical loading, these stabilized grains have been resilient against growth [34]. Comparatively, the Ni-P system, first reported to be NC stabilized by Kirchheim [15,35], achieves its stability through a thermodynamic stabilization method, with more recent work by Zhou *et al.* revealing the ability to vary the stability mechanism from thermodynamic to Zener through composition and/or process control [11].

Many nanocrystalline alloys, where the grains are not stabilized, reveal coarsening as a mechanism of deformation under loading [26–29, 36]. Under stabilization of an NC alloy, this removes GB migration as a deformation mechanism whereupon other mechanisms become dominant [10]. To identify and evaluate such mechanisms ideally requires *in situ* loading methodologies where one can observe the material response. By doing so, direct insights into the deformation and failure behavior can be gained, which are often speculated through *ex situ* tests with postmortem characterization.

A multitude of mechanical testing platforms have been developed for

* Corresponding author.
E-mail address: gthompson@eng.ua.edu (G.B. Thompson).

https://doi.org/10.1016/j.actamat.2023.119462
Received 18 May 2023; Received in revised form 1 October 2023; Accepted 23 October 2023
Available online 24 October 2023

such *in situ* experiments, ranging from commercially available systems [37–40] to independently developed microelectromechanical systems (MEMS) [17,18,41–48]. The observation of the deformation using these testing platforms can be through optical, X-ray, and electron microscopy methods, with each having various strengths and weaknesses. For optical imaging, image resolution for fine scale features is limited to sizes greater than a few hundred nanometers; in X-ray imaging, optical spatial resolution is of the order of a hundred nanometers; and for electron microscopy, it is dependent if the imaging mode being either scanning or transmission modes. This work will focus on transmission electron microscopy (TEM) because it has the highest spatial resolution, of the order of a few nanometers, which is ideal for NC stabilized alloys.

Of these TEM-based devices, the majority of studies focused on NC materials have been limited to mechanical loads applied at room temperature (RT) [17,18,47,48]. For example, Gupta *et al.* [48] employed stress relaxation tests to quantitatively extract the activation volume of nanocrystalline Au films while Guo *et al.* [39] and Kumar *et al.* [49] both examined grain rotation under mechanical loads within a TEM. If temperature is applied during loading, it is achieved through an attachment that heats the sample through the TEM, such as a laser [50–56] or the loading device itself [11,57,58]. Arguably, the latter method offers more flexibility in that a specialized TEM column is not required. Of the loading device approach, Zhu and his group [41] have constructed a MEMS chip that applies simultaneous thermal and mechanical loads on TEM specimens. To date, this device has been employed for the study of 1D nanomaterials such as Si or Ag nanowires [41,46,59]. Despite the variety of potential means to perform thermomechanical loading for *in situ* TEM, there has not been a significant number of reports examining NC alloys using this approach. Since load and temperature are both means to coarsen NC grains, their compound effect on nanostructure stability and strength offers an interesting opportunity for study. This work serves to bridge the gap between the mechanical and thermomechanical testing regimes within the TEM allowing for insights into nano-structural evolutions when these two types of loads are applied together.

In this paper two NC stabilized alloys are chosen for study: the ternary Ni-40Cu-0.6P (at.%) [60] and the binary Ni-40Cu (at.%) system (which serves as the control). The Ni-Cu alloy forms a solid solution with the Ni-40Cu composition being reported as the peak strength [61]. In the ternary system, the P solute partitions to the GBs and provides a thermodynamic stabilization mechanism between the two NC nanostructures [11].

2. Materials and methods

2.1. Fabrication of thin films

A set of Ni-40Cu and Ni-40Cu-0.6P (at.%) NC films were deposited via magnetron sputtering in an AJA 1500-F sputtering chamber by co-sputtering elemental Cu with either Ni or Ni-4P (at.%) targets, respectively. Prior to sputtering, a base pressure $< 4.0 \times 10^{-6}$ Pa was achieved wherein ultra-high purity Ar was flowed into the chamber at a rate of 10 standard cubic centimeters per minute while a gate valve throttled the pumping rate to achieve the working gas pressure of 0.267 Pa. Each film was deposited onto pre-polished 13 mm radius NaCl crystals at a deposition rate of 0.1 nm/s to a thickness of 75 nm. The NaCl substrates were then dissolved in deionized water allowing the film to float off the substrate and be suspended on the water surface. The liberated films were then lifted onto a 3 mm diameter Cu grid, dried via wicking, and prepared for FIB lift-out as outlined in [62].

The compositions used in this work were prepared through known sputtering rates calibrated by atom probe tomography (APT) in our prior work [59]. The compositions were verified via APT to within 0.1 at.%.

2.2. Description of MEMS devices

The MEMS device used here consists of a free-standing comb drive actuator that supports Z-shaped Si springs, Fig. 1. The central springs simultaneously support a viewing shuttle and provide Joule heating when connected to an external voltage supply. Equation 1 [41] describes the applied force, *F*, as a function of applied voltage, V (V):

$$F = \frac{N\epsilon t}{d} V^2 \tag{1}$$

where *N* is the number of comb pairs, ε the permittivity of the environment, *t* the device thickness, and *d* the spacing between adjacent comb pairs. A comprehensive description of the device design is provided in [41], with the primary changes here being the active device thickness and size to enable higher loads.

The Z-beams are modeled as ideal springs [41,42] allowing for calibration of the applied force through Hooke's Law. The spring stiffness was calculated by finite element analysis (FEA) on the ANSYS software platform with a temperature dependent model [63]. The temperature dependency of Si's Young's modulus is given as:

$$E(T) = E_0 - 0.04\ (T - T_0)\ \# \tag{2}$$

where E_0 (160 GPa) is the Young's modulus of Si at room temperature (T_0, 22 °C) and E(T) is the Young's modulus of Si at an elevated temperature. Each device was measured to assess the shuttle gap width as a function of the applied voltage and/or temperature prior to mounting a specimen based on a modeled spring stiffness of 204 $N{\cdot}m^{-1}$ at 22 °C and 197 $N{\cdot}m^{-1}$ at 150 °C. The upper bound temperature is limited by the elastic response of the Si-based device [63].

The devices were manufactured by MEMSCAP® via the Silicon-on-Insulator Multi-User MEMS Processes (SOI-MUMPS) with an active device thickness of 25 μm. Each device was evaluated under an optical microscope at 2000x magnification to ensure separation of features prior to use. For the interested reader, the details of this and similar MEMS chip devices are found in reference [64]. The devices were then Ag epoxied into a custom carrier fit to a Hummingbird 8-pin Electrical Biasing Holder and wire-bonded to the gold pads via 1 mil Au wire.

The thermoelectric and electromechanical responses were again modeled in ANSYS via a 3D multi-physics technique discussed in detail in reference [41]. Thermal modeling results were validated by measuring the resistance of the device while external heat was applied in a vacuum chamber up to 200 °C. This resistance was then compared to the intrinsic resistance of the device while heated through Joule heating. The model was additionally verified by qualitatively comparing the grain growth behavior of NC Pt on the MEMS device as compared to a DENS Solutions Wildfire® chip for a temperature range of 22 °C – 700 °C with further details of this calibration reported in the Supplemental section.

2.3. In situ loading procedures

Annealing ramp procedures were defined in terms of current per

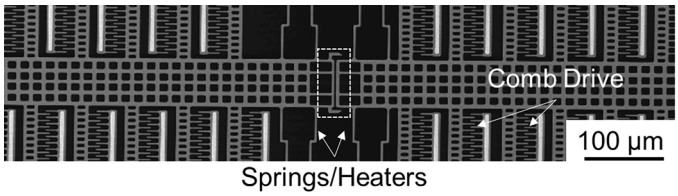

Fig. 1. Scanning electron micrograph showing the key features of the device. An electrostatic comb drive allows for mechanical loading. Specimens are welded across the central shuttle gap enclosed in the white dashed box. The entire structure is supported by Z-shaped beams which serve as springs and allow for resistive heating.

second rather than temperature because of the complexity of the electrothermal model. Furthermore, a linear current ramp rate does not result in a linear temperature rise with the reader referred to Appendix Fig. A1 for additional details relating the temperature as a function of time and current. The devices were heated at a ramp rate of 0.01 mA·s^{-1} to slowly bring the system to equilibrium. Specimens were held at the maximum loading current of 10 mA (150 °C) for 60 min. prior to applying mechanical loads to allow for stabilization of both the MEMS device and any microstructural evolution in the specimen. The specimens were then mechanically loaded at an assumed stress rate of ≈ 10 MPa·s^{-1}. This translates to a real stress rate of 3.75 – 5.38 MPa·s^{-1} applied to the specimen as measured in post-processing. The real stress rate applied to the specimen cannot be fully predicted due to specimen unfurling, slippage, and the actual percentage of the load that the specimen bears relative to the springs. However, the real measured stress rates can be captured during the expriment and are the following: Ni-40Cu at RT: 4.81 MPas^{-1}, Ni-40Cu-0.6P at RT: 3.75 MPas^{-1}, Ni-40Cu at 150 °C: 5.38 MPas^{-1}, and Ni-40Cu-0.6P at 150 °C: 4.29 MPas^{-1}. Further explanation for these calculations is provided in Appendix A1 with supplementary figures Fig. A2 through Fig. A4 added for clarity.

2.4. Microstructural characterization

Thin film specimens were prepared for TEM through a focus ion beam (FIB) milling lift-out technique using a Tescan Lyca XMU FIB-SEM. The samples were extracted from the plane-normal of the 75 nm thick films and shaped via an 8 keV, 120 pA Ga^+ ion beam for milling and an 8 keV, 20 pA Ga^+ ion beam for welding. The further details of the procedure are outlined in [62,65,66].

The nanostructure of the films was microstructurally characterized through the plane-normal during *in situ* studies in a 200 keV FEI Tecnai G^2 Supertwin TEM. These films were characterized at various stages including in the as-deposited state (no thermomechanical load condition), after a 60 min. annealing step, during thermomechanical loading, and post loading. During the loading steps, *in situ* videos were acquired at 10 frames per sec. to capture the material response as deformation occurred.

The grain size of the films was measured through dark field imaging within the gage section, with a minimum 150 grains counted per specimen.

2.5. Simulation details

To support the forthcoming structure-property discussion, atomistic NC structures were created and mechanically tested. These structures consist of nearly 40 grains, periodic boundaries, and have a grain size of 8 nm and a randomly selected grain orientation distribution. They were initially created for elemental Ni from phase field simulations using the methods outlined in [67] and equilibrated using a two-step equilibration approach [68]. This approach ensured that the resulting NC structures are more physical in terms of topologies and size distributions of grains and GBs and are also properly equilibrated. All simulations were performed in LAMMPS software [69] and visualizations carried in OVITO [70].

To date, there is not a well-vetted thermodynamic potential for the Ni-Cu-P alloy. However, Ni-Cu forms a complete solid solution [71] and Ni and Cu exhibit similar partition and reactive phase formations with P. To that end, we have employed the use of a Ni-P structure, which has an established potential [10], to assess the mechanical behavior as a function of NC stability to lend insights into experimental alloys' behavior. Alloyed Ni-P structures were generated from NC Ni structures by randomly replacing some amount of Ni atoms with P atoms to reach a global composition of Ni-1P (at.%). The initial alloyed structures were subjected to the hybrid molecular dynamics (MD) - Monte Carlo (MC) simulations until all the solute segregated to GBs and the system's potential energy reached a local minimum [72]. A MC step consisted of swapping P and Ni atoms with probabilities dictated by the Metropolis criteria at 23 °C (300 K). After every 1000 MC steps, the whole system was equilibrated for 1 ps at 23 °C in an isothermal-isobaric ensemble while maintaining zero normal pressure at periodic boundaries [10]. Interactions in elemental Ni and alloyed Ni-P structures were modeled using EAM style interatomic potentials that are shown to reproduce experimental lattice parameters and cohesive energies [73,74].

With the system constructed, the NC Ni and Ni-P structures were then tested under uniaxial tension using MD simulations in an isothermal-isobaric (NPT) ensemble at a constant strain rate of 10^8 s^{-1} at 23 °C temperature and zero normal pressure along boundaries in the transverse directions. The stress values between 5 and 10 % strain were averaged to obtain the flow stress. To simulate fracture, the uniaxial tension MD simulations were also performed in canonical (NVT) ensemble at 23 °C and 150 °C temperatures. The contribution of deformation mechanisms was quantified as percentages of total loading strain accommodation during the uniaxial tensile testing using continuum scale kinematic metrics [75,76]. Atoms participating in different deformation mechanisms (*i.e.*, twinning, dislocation, elastic grain deformation and GB deformation) can be delineated based upon the kinematic signatures like slip vector, shear and structural environments [75] with additional details regarding this found in [10,77]. The relative contribution of the GB mechanisms and all the intragranular mechanisms combined (*i.e.*, twinning, dislocation, elastic grain deformation) is obtained as the ratio of percentages of total loading strain accommodated in these two mechanisms averaged over the flow regime (*i.e.*, 5–10 % strain).

2.6. Digital image correlation

Digital image correlation (DIC) was applied to the last 60 s. of deformation before the films failed. While DIC is based on contrast tracking and dynamical diffraction in a TEM can confound image interpretation, this was not found to be a significant issue and will be further discussed later in the paper. First, frames were stack aligned in AstroImageJ 5.0.0.00 using an image stabilizer algorithm. The transformation was defined as a translation with a maximum pyramid level of 1, template update coefficient of 0.9, and error tolerance of 1×10^{-7} for a maximum of 200 iterations. The stacked images were exported from AstroImageJ and imported into the VIC-2D7 software suite for DIC analysis. The region of interest (ROI) was defined and a subset size evaluated for each specimen individually. The image correlation map was then calculated using an exhaustive search procedure which filled the boundaries of the ROI with a low-pass filter. The search applied Gaussian weights to the subset with an optimized 8-tap interpolation approach using a normalized squared differences criterion. The Lagrange strain was calculated for the mapped region resulting in strain maps. The maps are scaled to the minima and maxima of the specimens across the 60 s. range. As defined in the experimental section, loading rate was ≈ 3.75 – 5.38 MPas^{-1}, meaning that the analyzed time frame corresponds to a 225 – 323 MPa load range, depending on the specimen, prior to failure and the Lagrange strain is calculated with respect to this frame rather than the initial undeformed configuration.

3. Results & discussion

3.1. Mechanical & microstructural properties

Each specimen was mechanically loaded at a stress rate of 3.75 – 5.38 MPa·s^{-1}. Stress is calculated from a force based on the smallest gage width of the individual specimen (which ranged between 400 – 500 nm) and a gage thickness of 75 nm determined by the deposition rate of the specimen with further details provided in Appendix A1. Note that the thermomechanically loaded specimens are subjected to a slight stress offset in the pre-load condition because of the thermal expansion of the Si device applying a minor tensile load.

Fig. 2(a-d) are plots of the two alloys at the two temperatures. Strain measurements are made by manually measuring the shuttle gap width at periodic intervals (30 s.). These manual measurements are prone to error because of specimen geometry, unfurling of the specimen during the initial loading stage, and slippage from the grips. When a specimen is initially loaded, large initial jumps in the far-field strain are observed until the specimen is pulled taut under loading. This is clearly seen in the Ni-40Cu alloy loaded at 150 °C, Fig. 2(c), where the first 30 s. of data returns a 2 % far-field strain under a load of only 0.14 GPa. Additionally, the Pt welds attaching the specimen to the shuttle may allow some slippage to occur between the specimen and the weld joint. For our experiments, accounting for this slippage event does not substantially alter the failure trends across the various conditions. Nonetheless, an example of this slipping behavior is noted in the Ni-40Cu-0.6P alloy loaded at 150 °C in the micrographs that will be presented in Section 3.2.2. Collectively, these effects contribute to error in the reported strain. Collectively, one should carefully consider these effects when assessing the far-field strain value provided in the stress-strain plots in Fig. 2(a-d), which is an outcome of experimental limitations using this testing method. While these are practical experimental issues, the ability to monitor the specimen response under loading, even with semi-quantitative measurements, provides the opportunity for new insights to deformation evolution to loading and compliments "bulk" scale testing that are more appropriate for more rigorous mechanical property evaluation which cannot capture the mechanistic behavior.

The Ni-40Cu-0.6P / room temperature (RT) alloy shows a fracture stress of ≈ 1.91 GPa. Upon thermomechanically loading, the fracture stress lowers to ≈ 1.80 GPa, which is 94 % of RT fracture strength. The decrease in strength at fracture can in linked to two potential outcomes. First, in the RT test specimen, in principle, all the species are in solution in the as-deposited condition, with Zhou *et al.* noting that only a minor amount of P is found in the GBs [11]. Only upon post-processing annealing does the P solute partition significantly into the GB regions. Prior work by the authors [60] reveals the highest hardness (9.69 ± 0.09 GPa for Ni-40Cu-0.6P) occurs when all the solute is providing solid solution strengthening. Upon annealing, the P partitions to the GBs to stabilize the NC structure against grain growth but this results in a loss of P's contribution to the solid solution strengthening evident by a reduction of hardness to 9.11 ± 0.1 GPa. Furthermore, when heat is applied to drive the solute into the GBs, some modest grain growth

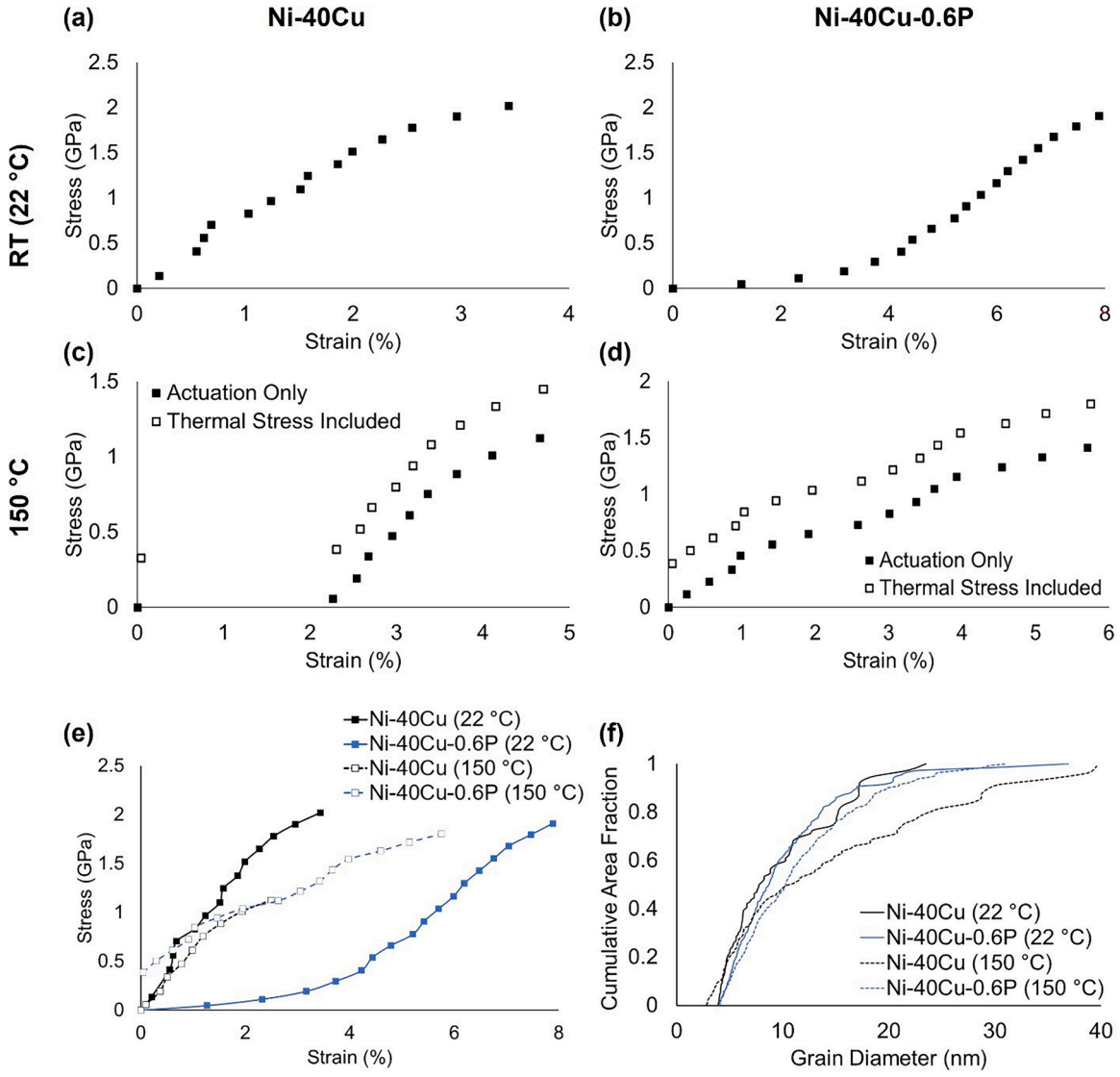

Fig. 2. Mechanical and microstructural properties measured during testing of the NC foils. Stress-strain and force-time plot of **(a)** Ni-40Cu at RT; **(b)** Ni-40Cu-0.6P at RT; **(c)** Ni-40Cu at 150 °C; **(d)** Ni-40Cu-0.6P at 150 °C. Cumulative plots for all specimens: **(e)** corrected stress-strain curves for all conditions; **(f)** initial grain size distributions measured by dark field techniques. (For interpretation of the references to color in this figure legend, the reader is referred to the web version of this article.)

occurs, Fig. 2(f), before stabilization when one compares the average values prior to mechanically loading the foils. But any growth is minimal evident in the overlapping standard deviations about each average. Here, the Ni-40Cu-0.6P / RT sample has an average grain size of 8 ± 4 nm and the Ni-40Cu-0.6P / 150 °C sample has an average grain size of 10 ± 8 nm, with the higher standard error value after annealing being because of inhomogeneous coarsening. Thus, the loss of the P solute out of the matrix to the GBs coupled with a modest increase in grain size contributes to the measured reduction in loss of strength when loaded at temperature.

To readily compare the two compositions in the four temperature conditions, Fig. 2(e) plots the stress vs. strain of all data sets with correction for initial unfurling of the Ni-40Cu alloy loaded at 150 °C. The uncorrected data and further discussion of data corrections and

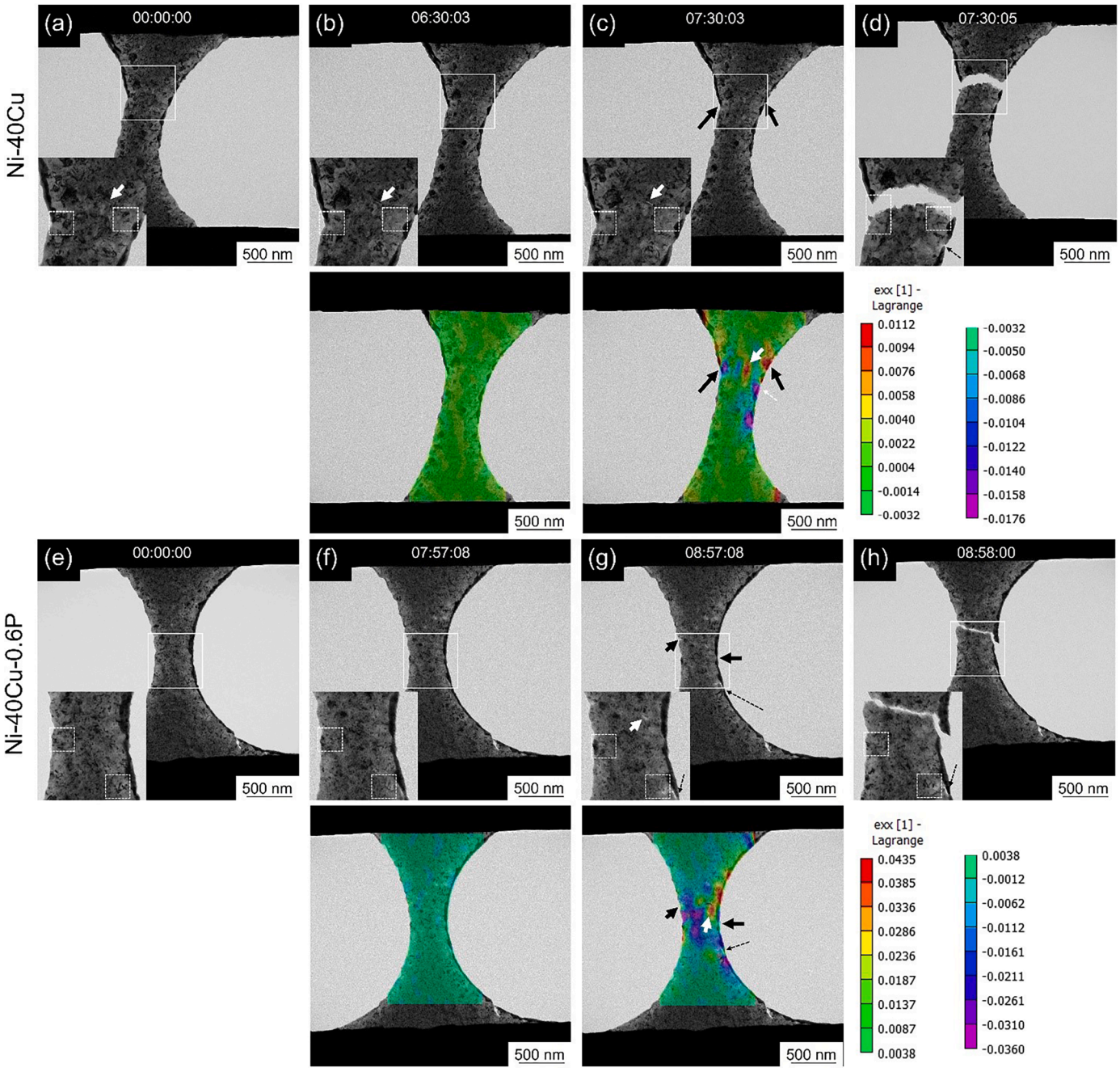

Fig. 3. Brightfield micrographs of those films during loading at 22 °C. Timestamps are displayed in mm:ss:ms. Beneath the unloaded and near-fracture maps are DIC maps for the hydrostatic strain in the load direction which highlight microstructural transformations. Dashed boxes within the inset images display regions of interest. **(a)** Ni-40Cu as-deposited and prior to loading where an interior crack is observed as-deposited (white arrow); **(b)** Ni-40Cu 60 s, at an applied load of 1.78 GPa, before failure; **(c)** Ni-40Cu just before failure, at an applied load of 2.02 GPa, where two cracks have developed on the exterior of the film (black arrows) and changes in diffraction contrast are seen within the dashed boxed regions; **(d)** Ni-40Cu just after fracture where the fracture has followed the interior crack lines and a very small nano-scale crack has developed (dashed black arrow) upon fracturing; **(e)** Ni-40Cu-0.6P Ni-40Cu-0.6P as-deposited and prior to loading; **(f)** Ni-40Cu-0.6P 60 s, at an applied load of 1.68 GPa, before failure; **(g)** Ni-40Cu-0.6P just before failure, at an applied load of 1.91 GPa, where two cracks have developed on the edges of the film (black arrows) and one in the interior of the film (white arrow) with changes in diffraction contrast highlighted in the dashed boxes; **(h)** Ni-40Cu-0.6P just after fracture where the fracture line passes through the top-left exterior crack and the interior crack from **(g)** and a residual crack remains (black dashed arrow). (For interpretation of the references to color in this figure legend, the reader is referred to the web version of this article.)

artifacts is found in Appendix A1.

For the control Ni-40Cu / RT, the fracture strength is ≈ 2.02 GPa and upon testing at 150 °C, the fracture strength is ≈ 1.12 GPa, which is 55 % of RT fracture strength. The strength measured at RT is comparable to that of the ternary alloy as P in the Ni-40Cu-0.6P alloy has not yet strongly partitioned to the GBs. Based on the work of Bikmukhametov *et al.* [78], the addition of 0.6P would increase the relative strength of the ternary alloy by approximately 8 %. The difference in strength between these two alloys at RT is within the error given the numerous limitations in gathering the measurement as discussed above. More interestingly, there is a substantially higher percentage reduction in strength with temperature in the binary alloy than the ternary one. This can be explained by solute P partitioning to and strengthening the grain boundaries of the Ni-40Cu-0.6P alloy at elevated temperatures [60]. The reduction of strength in the binary Ni-40Cu upon heating is linked to its increase in grain size from 8 ± 5 nm (RT) to 18 ± 11 nm (150 °C) prior to loading. This average grain size value is nearly double of the NC stabilized counterpart at the same test temperature, though noting that each of the average grain size values are within each other's standard error.

The most notable outcome of this data set is the significant retention of strength upon thermomechanically loading the NC stabilized ternary alloy. Collectively, these results demonstrate superior strengthening that can be achieved through NC stabilization.

3.2. Deformation and failure behavior

With the strength responses measured, the advantages of doing such tests *in situ* to characterize the nanostructure evolution and failure behavior is presented. The DIC videos for the *in situ* acquisitions of each test are provided in the Supplemental section available online with this paper.

3.2.1. Room temperature response

A series of still frame bright field images taken from the *in situ* video acquisition for the RT loaded specimens is displayed in Fig. 3. This series shows the films in the unloaded state, Fig. 3(a,e), 60 s. before failure, Fig. 3(b,f), just before failure, Fig. 3(c,g), and just after failure, Fig. 3(d, h). A careful review of the outer edges of the gage section reveals dark, diffraction contrast for a series of larger grains. FIB milling to shape the gage length is known to create ion induced grain growth [62,79] and explains this artifact; however, this FIB induced coarsening is qualitatively less in the Ni-40Cu-0.6P samples which is attributed again to the presence of the stabilizing solute. This coarsening is important to recognize when considering grain size effects on the ultimate tensile strength reported herein, as the grain size values reported are averaged over the entire sample with generally coarser grains on the exterior. While this sample has not been annealed to induce the P solute partitioning, prior atom probe tomography characterization by the authors has shown some slight partitioning of the P to the GBs in the as-deposited state which is provides some modest stabilization from the ion-induced grain growth [11,72]. And, finally we note the presence of such specimen preparation induced coarse grains may also contribute to the lower failure strength of the binary alloy as compared to the ternary because of their comparatively larger volume fraction between the two samples.

Located at the bottom, left-hand corner of each of these bright field micrographs are magnified insets of the regions noted by the solid white box in each image. Within these insets, dashed white boxes are added to draw the eye to the same region and highlight the microstructural evolution that occurred between each of the selected still frame images. The dashed boxes note a few (but not all) areas subjected to grain contrast changes, with a particular grain in that box coming in or out of contrast. Since contrast is linked to diffraction, this indicates that the granular crystallite orientation to the electron beam has shifted. Such shifts can be a result of grain coarsening or grain rotation. The thick arrows in these frames are guides to features through which the fractures pass. Thick white arrows point to cracks while black arrows point to the edges of the fracture line.

While bright field images are useful, the ability to readily observe all contrast changes over the entire sample over a multitude of video frames (>10,000 frames gathered over the course of the experiment) is difficult, if not impossible, to examine manually. There is a high likelihood that some features will be missed. Furthermore, after fracture, one is often biased to the observations that solely focus on where the particular region of failure occurred. To mitigate these concerns, DIC has been employed.

Traditionally, DIC is used in optical microscopy where a speckle pattern is applied to the specimen surface to allow for tracking features for the purpose of strain mapping [80,81]. This same idea has also been applied using scanning electron microscopy (SEM) measurements [82–86]. However, unlike an optical image, where all the contrast from these features are collected at the same time since its parallel illumination, the SEM image is a serial sequence since the beam rasters over the sample creating an image delay from the first captured point to the last captured point. In contrast, an advantage of the TEM, like an optical microscope, illumination of the sample uses parallel rays and collects the entire image at the same time.

DIC has been previously employed to *in situ* TEM deformation studies [87,88], where the samples were amorphous and the Bragg diffraction contrast would be minimal to reduce artifacts in contrast tracking/strain mapping. Here, the same DIC idea is applied, but now to a NC alloy. The presence of a crystalline phase, in principle, will increase the potential contrast error in tracking since the crystallites can rotate in and out of contrast resulting in aberrant strain maps. While this is a legitimate concern, Wang *et al.* [87] did capture the DIC of their amorphous sample by using the native contrast that comes from short range ordering and here the NC grain size does spatially limit the extent of long range ordering.

If there is a significant change in contrast because of grain rotation or coarsening, this would result in a loss of data as calculated by the DIC map [80]. Thus, the hydrostatic strain maps presented for the load direction (e_{xx}), Fig. 3, provide a reasonable evaluation of the localized strain, as grain rotation and growth events should not contribute to the strain map as they would instead result in a failure in indexation. Noting that determination of the largest pixel size above which the indexation fails is user defined, one ideally would use the smallest size for the best spatial resolution without oversampling the image. The shear strain components, e_{xy}, provide less insight into structural transformations than the hydrostatic component and are provided in Appendix Fig. A5for completion. Here, DIC is used as a data mining tool to identify regions of localized deformation; however, we noted that the DIC hydrostatic strain map matches well with microstructural evolutions. In the supplementary online video section, an overlay of the DIC contrast from the sample during pulling is provided for both the hydrostatic component in the loading direction (e_{xx}) and the shear component (e_{xy}).

While the sample is crystalline and is subject to the diffraction contrast concerns noted above, the level of contrast changes throughout the sample, particularly in the early stages of loading, was found to be relatively minor, evident by the continuous green contrast that is seen in the DIC image under its corresponding bright field image in Fig. 3. In the supplementary videos, there is a flickering of light green contrast during the pull supporting that any error created by these dynamical diffraction effects are present but not overwhelming in using DIC as a tracking method. When the sample approaches the stress at failure, specific regions in the sample indicate significant changes in contrast. These are the darker blue, purple, red and yellow strain contrast signals see in Fig. 3. These regions directly correlate to where the film is undergoing significant deformation and where the sample ultimately undergoes failure. For example, in Fig. 3(c), in the inset image, a thick white arrow in the middle of this image points to the onset of a crack in the interior of the NC alloy. The corresponding DIC image below showing a region of

high contrast evident by the red strain pointed to by the matching thick white arrow. In this same sample, the thick black arrows in the DIC image of Fig. 3(c) correspond to the sample's ultimate fracture path. While other areas in the DIC image also show contrast (see the thin dashed white arrow where a crack develops, for example), these were not the failure points. Comparison of these regions to the bright field video images is found to have the onset of microcracking or other changes in the grain contrast. Collectively the use of DIC readily helps identifying various regions of deformation, even those areas that did not result in catastrophic failure. Through the video sequence of DIC images, the initial formation and subsequent evolution of these regions are now more apparent than what one can be easily gleaned through simple viewing of the bright field image sequence.

With the DIC mapping, the next question is if the measured strain values from the map are accurate. Here, the authors first note that far-field strain values extracted from the DIC maps, reported in the respective discussions below, showed only slight variation to the manually measured far-field strain using the shuttle seperation for the same time frame (60 s. before failure). The difference between the two techniques is unsurprising with manual measurements generally reporting higher strain values than DIC due to the inclusion of slippage from the grips. If the sample slips, the device has moved further than what the sample has responded and therefore measurement across the device gap overestimates the real strain in the sample. The high local strain gradients reported may be further influenced by the inclusion of out-of-plane stresses such as those created on the specimen from a few nanometer difference in shuttle height on either side of the gap when the specimen is pulled in tension.

As noted previously, the DIC frames analyzed the last 60 s. before failure. Computationally, it is impractical to do this analysis over the entire number of frames for the experiment. Thus, the strain changes shown for all the DIC maps are relative to the first frame of selected analysis to the last frame before failure within this 60 s. time sequence. Thus, the strain values from DIC would not match those from the strain values reported in Fig. 2, which is collected over the entirety of the loading experience.

In Fig. 3(c)'s DIC image, the maximum identified strain, which is also in the region where failure initiated, is $\approx$ 1.1 %, *i.e.*, the red tint on the outer edge of the gage section. However, the far-field strain measured by DIC corresponds to only 0.21 % $\pm$0.01 % strain across the map. Comparatively, manual measurement of the far-field strain for the same time period (60 s before failure) yield a strain of $\approx$ 0.89 %, which is reasonably close to the far-field strain computed by DIC given the differences in measurement techniques. This example is the worst case, whereas most of the other far-field strain values are closer to each other as is described below. For example, the Lagrange strain is independent of rigid body motion while the far-field strain is simply a small-strain tensor.

Next, the DIC strain map corresponding to the ternary alloy is considered, Fig. 3(g). The algorithm reports a maximum strain region of $\approx$ 4.4 % with a far-field strain of 1.00 % $\pm$0.02 %. Again, using the same frame sequence in the last portion of the test, manual measurement of the far-field strain yields a value $\approx$ 0.84 %, which is in good agreement when considering the same time interval. Note that Tong *et al.* [81] have optically measured strain variations in materials and commented that local strain measurement can be higher than the overall strain measured, even on the order of 6 – 7 times higher. If one further investigates the DIC contrast color scheme of Fig. 3(f), particularly the other side of this high strain region, it is balanced by a localized strain region of $\approx$ −3.6 % (purple) with much of the balance of the sample strained being colored values that are $\pm$ 1 %.

Regardless of these collective issues where matching variation occurs, DIC is showing, at least qualitatively, a means to identify the regions of deformation in the crystalline material by TEM image capture. Furthermore, the strain measurements, both by the device and DIC mapping, are on the order of magnitude for values expected from mechanically tested metal thin films [89–91] and offers areas for future investigation and optimization. For the balance of the paper, where DIC is used, it is presented as a mining tool to locate the regions of interest of where and how these nanostructures evolved under load.

Using the DIC as a guide, examination of the binary Ni-40Cu alloy reveals the growth of two sets of internal cracks, Fig. 3(c). Comparing the inset image dash boxes between Fig. 3(b) and (c), one can see a reduction of diffraction contrast at the edges of the gage length between these two frames. This lighter contrast region is correlated to the DIC image where the thick black arrows highlight the regions that ultimately indicate where the fracture will occur. This fracture path follows the internal crack that has formed in this structure suggesting a potential initiation site wherein it would then be transverse to both sides of the gage length.

Like the binary Ni-40Cu, the ternary Ni-40Cu-0.6P alloy develops cracks during mechanical loading. These cracks form at the edges of the specimen and in the interior of the film, *i.e.*, the thick white arrow in Fig. 3(g). Examination of the microstructural features near the fracture site reveal a less clear change in diffraction contrast in this ternary alloy, Fig. 3(g), as compared the binary one, Fig. 3(c), with the image correlation technique highlighting areas of microstructural activity below each of the micrographs. A crack in the bottom-right side of the inset image indicated by a white dashed arrow in Fig. 3(g) can be correlated to an area surrounded by compressive strains in DIC map (purple colored region). Internal crack formation is also noted in an area of tensile (red) contrast, noted by the thick white arrow in Fig. 3(g). Nearby, other microstructural evolution events occur which are difficult to resolve by the eye, but the DIC map once again does an excellent job of revealing these changes. One can make out slight changes in grain size and contrast throughout the central section of the gage width by comparing the insets in Fig. 3(f,g).

With the sample broken, the fracture surfaces of the Ni-40Cu and Ni-40Cu-0.6P specimens, pulled at RT, are now examined and found to be an intergranular failure mode, Fig. 4. This is confirmed by the rough edges of the fracture surface outlining the grain boundaries. The Ni-40Cu alloy also exhibits a larger, lighter-contrast region along the fracture surface. This corresponds to individual grains within the alloy that have slid across one another being pulled out to reveal a thinner, electron transparent region (lower thickness contrast), Fig. 4(a). Comparatively, the Ni-40Cu-0.6P alloy shows a finer, jagged toothed profile with fewer areas of this type of lighter contrast along the fracture surface, Fig. 4(b). This indicates that fewer grains in the ternary alloy, as compared to the binary alloy, slid across each other during the pulling. This difference is linked to the P solute acting as a GB strengthener from sliding and/or decohesion.

3.2.2. Room temperature modeling

Atomistic simulations of the strength of NC Ni and Ni-P under uniaxial tension for 8 nm grain size structures is presented in Fig. 5. This is at the same size as our experimental grains. The aim of these simulations is to ascertain the influence of the P on the GB strength. Again, it is noted

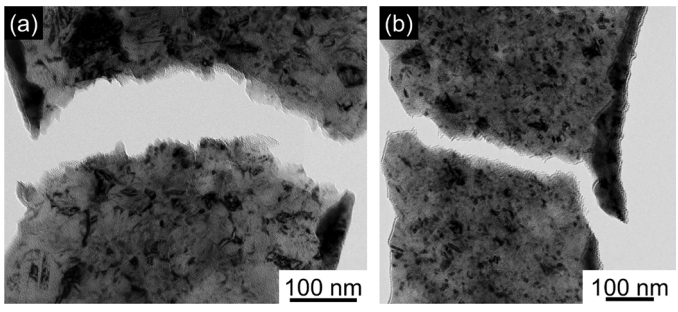

Fig. 4. High magnification brightfield micrographs stitched together **(a)** the fracture surface of Ni-40Cu and **(b)** the fracture surface of Ni-40Cu-0.6P.

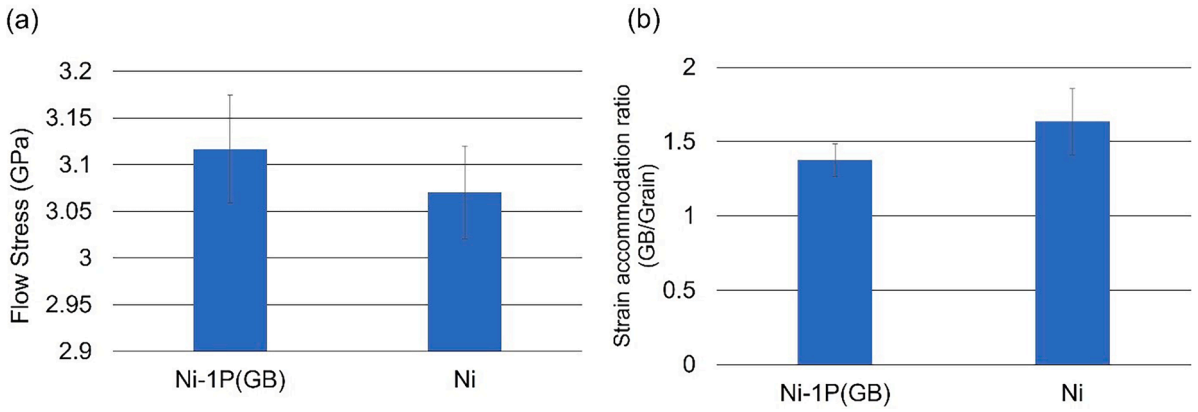

Fig. 5. Bar graphs showing how the flow stress **(a)** and strain accommodation distribution **(b)** vary with solute content and distribution for Ni and Ni-1P with an 8 nm grain size under isothermal-isobaric load. (For interpretation of the references to color in this figure legend, the reader is referred to the web version of this article.)

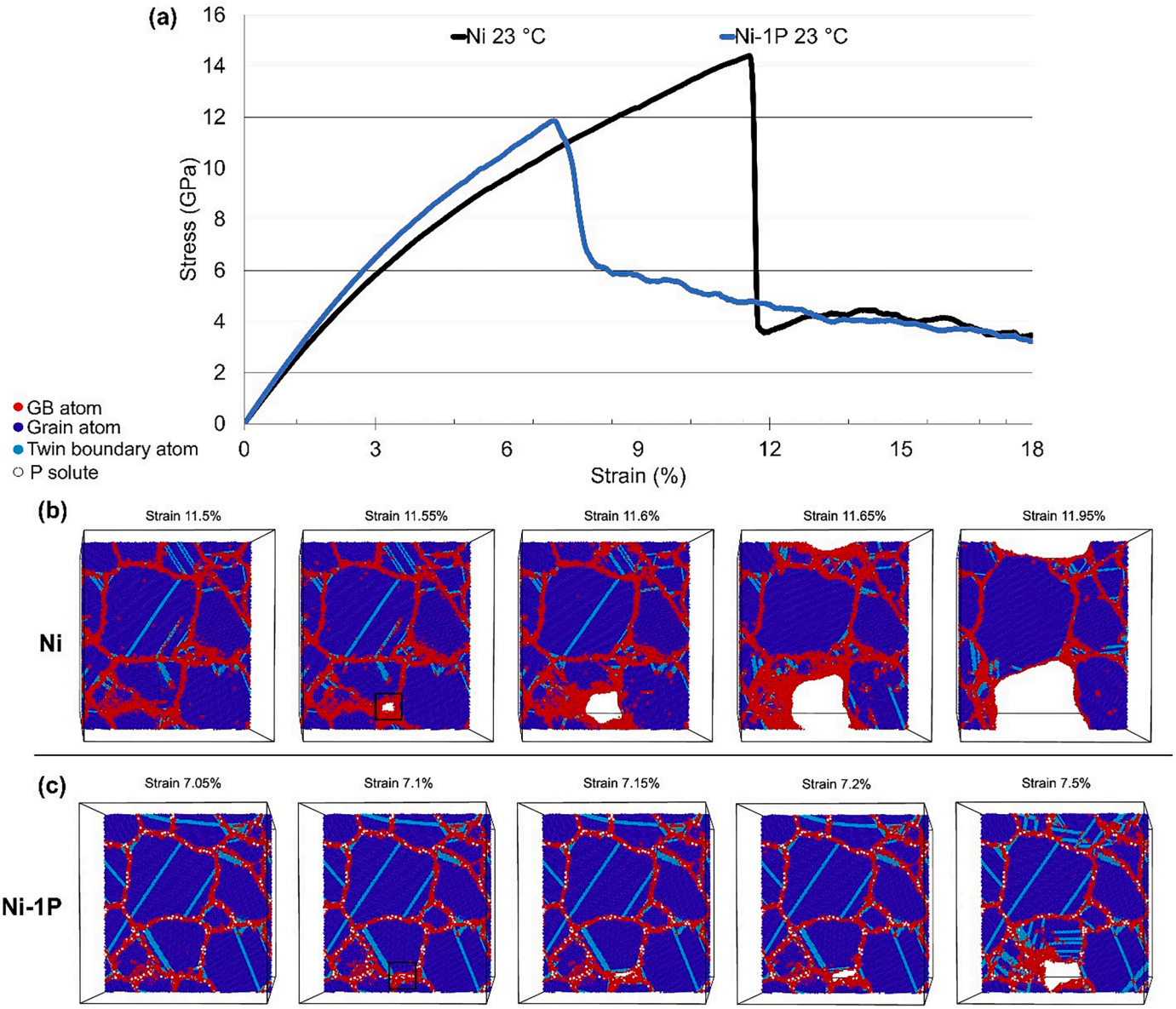

Fig. 6. **(a)** A stress-strain plot showing the failure behavior of Ni and Ni-1P with an 8 nm grain size under isothermal-isovolumetric load. Beneath are 2D slices through **(b)** the elemental Ni structure as it fails, and **(c)** the Ni-1P structure as it fails. Black boxes enclose the nucleation site of the crack in the first frame that the crack has formed. (For interpretation of the references to color in this figure legend, the reader is referred to the web version of this article.)

that Ni and Ni-P are modeled rather than Ni-Cu and Ni-Cu-P because of the lack of good thermodynamic potentials and the development of such thermodynamic potentials beyond the scope of this work. And, as commented above, Ni and Cu form a complete solid solution [71] and the thermodynamic behavior of P is similar between Ni and Cu [92–94] suggesting that these simulation results will be reasonable estimations.

What can be gleaned from the NPT condition, displayed as bar graphs in Fig. 5(a,b), is that the flow stress increases as P is added to the GBs of elemental Ni. Experimentally, even in the as-deposited (solutionized) state, there will be some P located within the GBs [10,11] which would promote an increase in flow stress in the Ni-40Cu-0.6P alloy as compared to the Ni-40Cu alloy. As previously noted, prior experimental work has shown the potential for solid solution strengthening as P is added to the grain interior of Ni or Ni-Cu [60].

The flow stress of a NC material is dictated by the competition between the GB and the intragranular mechanisms towards microstructural strain accommodation [10]. The increase in flow stress as P is added to the GBs, Fig. 5(a), is indicative that the solute is indeed strengthening the boundaries. This is further supported by comparing the GB to grain strain accommodation, Fig. 5(b). The ratio being greater than unity indicates that GB mechanisms are the dominant deformation mode for this smaller grain size and these GBs accommodate more strain than the intragranular mechanisms, in agreement with previous studies [10]. The ratio decreases when the solute P is added to the GBs, which in combination with the increase in flow stress, would imply that the GBs are stronger in Ni-1P than in elemental Ni. This partially explains why the P containing alloy experimentally tested here (Ni-40Cu-0.6P) yielding a finer, jagged tooth pile than the Ni-40Cu alloy. Here, the boundaries were strengthened by the addition of P making them harder (and by default brittle) resulting in a more cleaved-like fracture behavior. In contrast, the alloy with no P had weaker GBs which resulted in cracks growing more coarsely through the GBs and ultimately a coarser fracture edge structure.

Further confirmation of the failure behavior is shown in Fig. 6, in which the modeled stress-strain plots for Ni-1P and Ni are displayed, Fig. 6(a), along with 2D slices through the structures during failure, Fig. 6(b,c).

Here, the model suggests that the Ni-1P alloy (again, with P forced into the GB) should fail well before the elemental Ni structure, Fig. 6(a). This appears to agree with the experimental data, Fig. 2, in which Ni-40Cu-0.6P is slightly weaker than Ni-40Cu. A more careful consideration of the modeled stress-strain plots reveals that the Ni structure can accommodate more stress and strain before a crack nucleates than the Ni-1P structure. However, the nucleated crack propagates more rapidly through the Ni structure than the Ni-P structure, was initiated as indicated by the steep drop off in stress at failure in the Ni structure, Fig. 6(a).

Slices through the failure event, Fig. 6(b,c) reveal a dramatic difference in the failure behavior between the Ni and Ni-1P structures. Atoms are color coded for ease of visualization – red atoms are considered part of a GB, dark blue atoms are considered part of the grain interior, cyan atoms comprise twin boundaries and stacking faults (hexagonal close packed), and white atoms (only visible in the GBs of the Ni-1P structure) are P solute atoms.

Looking first at the modeled Ni structure, crack nucleation initiates at a strain value of 11.55 %, Fig. 6(b). As the strain further increases, the crack grows substantially, even with only a 0.05 % increase. A secondary crack then impinges at the top of the modeled structure at 11.65 % strain and by 11.95 % strain, large sections of the structure have separated. The crack that nucleated at 11.55 % strain dramatically opens the structure across the 0.40 % strain differential across the sliced images.

Examination of the modeled Ni-1P system simulation reveals a significantly different progression of the crack as the strain progresses, Fig. 6(c). Here, the crack nucleates at a strain value of 7.1 %, grows very slightly with an increase in strain even up to 0.4 % strain higher than the initiation site. Ultimately the Ni-1P structure accommodates a larger strain differential after crack nucleation than the elemental Ni structure.

This difference in how much strain can be accommodated by the system before failure but after crack nucleation is significant to the experimental observations in Section 3.2.1. The model suggests that crack nucleation is harder to achieve in elemental Ni than in the Ni-1P binary system, but easier to propagate through Ni than through Ni-1P once it has formed. Fabrication of an idealized structure is difficult and elemental Ni reportedly deposits with significant void formation [95] depending on the deposition condition. In these films, nanoscale cracks preexist in the as-deposited state, which can be seen in Appendix Fig. A6. While the model appears to smoothly support the experimental results, the *in situ* data is vital to understanding why such differences in failure strength exist. The combination of *in situ* experiments to elucidate nanoscale cracks leading to the intergranular failure behavior with atomistic modeling suggests that the impact of such 2D defects, while often overlooked, are substantial in the processing NC alloys for structural applications. Furthermore, the modeled results displayed in Fig. 6 (b,c) of the different types of opening structure upon crack propagation are supportive of the fracture surface shown in Fig. 4, wherein the Ni-40Cu-0.6P alloy displays a finer-toothed edge than the Ni-40Cu deposit.

3.2.3. Thermomechanical response

A series of bright field micrographs acquired prior to and during thermomechanical loading is displayed in Fig. 7. The series consists of the alloys as-deposited, Fig. 7(a,f) upon annealing at 150 °C for 60 min., Fig. 7(b,g), 60 s. before fracture, Fig. 7(c,h), just before fracture, Fig. 7 (d,i), and just after fracture has occurred, Fig. 7(e,j). Ion beam induced grain growth is again noted along the edges of these films, Fig. 7(a,f), and has previously been explained in the results above. Some microstructural evolution is observed in both the binary Ni-40Cu and ternary Ni-40Cu-0.6P alloys, Fig. 7(a,b) and (f,g). These changes are supported by the grain size measurements noted in Fig. 2(f) where the Ni-40Cu alloy increased from 8 ± 5 nm at RT to 18 ± 11 nm at 150 °C while the Ni-40Cu-0.6P alloy increased from 8 ± 4 nm to 10 ± 8 nm under the same conditions.

Magnified insets of the white solid boxed regions in the bottom left-hand corner allow for easier evaluation of these microstructural changes. White dashed boxes within the inset images provide for similar areas to draw comparisons. Within these boxes, a change in diffraction contrast is noted during thermomechanical loading, which indicates a shift in grain orientation from either rotation or coarsening. Note that what appears to be a large grain in the ternary Ni-40Cu-0.6P alloy, Fig. 7 (f-j) on the right side of the gage section (pointed out by a small black arrow) is an artifact from a section of the film that has folded over during milling. Additionally, this ternary specimen slips noticeably away from the shuttle during loading, Fig. 7(g-j), and snaps back into place when the load is alleviated. This behavior implies that the foil is slipping out from the Pt weld during loading resulting in a lower specimen failure strength than what is reported and demonstrates the practical experimental complications for these types of *in situ* microscopy tests. Thick black arrows are also provided in Fig 7(d,i) indicating where the fracture line passes through upon failure.

As with the RT tests, the DIC maps in Fig. 7 guide the analysis of where these films failed and other notable regions of interest. The change in color from green in the RT loading condition to blue in these conditions is derived from a change in the scale bars. The Ni-40Cu shows a dark blue flickering of the DIC derived contrast during most of the loading procedure. Areas under high stress develop as the film approaches failure, evident by the red, green, and purple contrast spots in Fig. 7(d). The bottom-left tensile strain (red spot) is related to the bottom-left dashed box in the corresponding bright field micrograph inset in Fig. 7(d). A reduction in contrast is observed because either grain growth, rotation, or local thinning effects or a combination of these has occurred. Interestingly, no crack formation is observed prior to failure within the gage section or at the edges of the film. The specimen

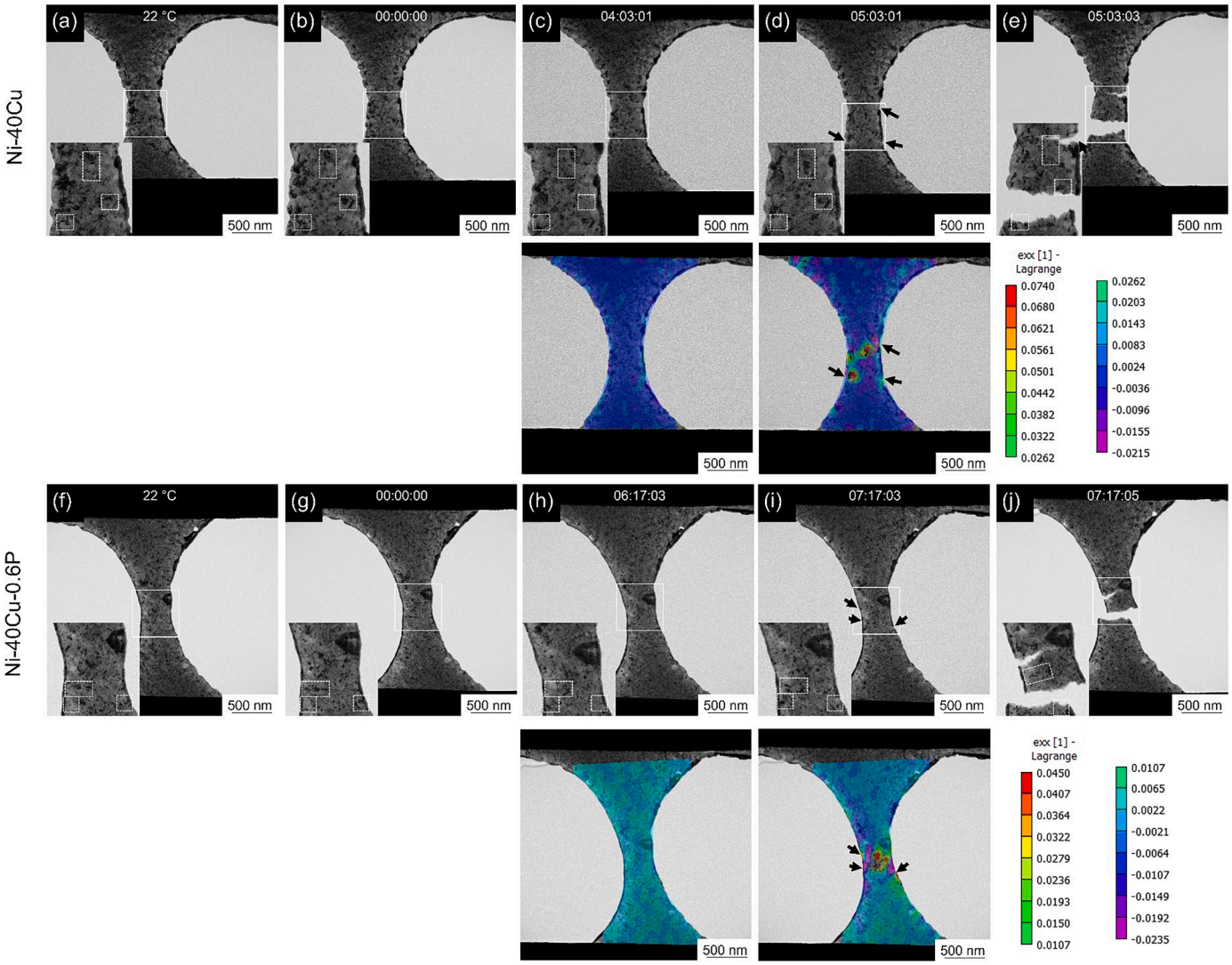

Fig. 7. Brightfield micrographs of those films during loading at 150 °C. Timestamps are displayed in mm:ss:ms. DIC maps for the hydrostatic strain in the load direction are provided below the unloaded and near-fracture micrographs to highlight areas of microstructural evolution. **(a)** Ni-40Cu as-deposited prior to annealing; **(b)** Ni-40Cu just after annealing; **(c)** Ni-40Cu 60 s, at an applied load of0.89 GPa, before failure; **(d)** Ni-40Cu just before fracture, at an applied load of1.13 GPa, where a small crack is noted (thick arrow) and a region of lighter contrast has developed **(b). (e)** Ni-40Cu just after fracture. A secondary fracture line is noted to transmit halfway through the specimen from the crack in **(d); (f)** Ni-40Cu-0.6P as-deposited prior to annealing; **(f)** Ni-40Cu-0.6P just after annealing; **(h)** Ni-40Cu-0.6P 60 s, at an applied load of1.63 GPa, before failure; **(i)** Ni-40Cu-0.6P just before fracture, at an applied load of1.80 GPa, a light-contrast region has developed with a very small nick and a very small nick has developed; **(j)** Ni-40Cu-0.6P just after fracture where the primary fracture passes through the small nick on the bottom-right side in **(i)** and a secondary fracture line is noted to transmit halfway through the specimen from the light contrast region on the middle-left side of **(i)**. Comment on (c) and h). (For interpretation of the references to color in this figure legend, the reader is referred to the web version of this article.)

ultimately fails in two locations, Fig. 7(e). The primary fracture (defined as transmitting through the entire gage width) passes through the localized tensile strain found in the bottom-left side of the DIC map, Fig. 7(d). A secondary fracture transmits halfway through the structure, passing through both the central tensile (red) area and a local compressive (purple) region nearby, Fig. 7(d). These regions are accompanied by significant changes in contrast, as noted by the inability of the DIC map to find a solution in the area and mapping the color as black. Regarding this secondary crack, it is important to note that in the video capture sequence, the hardware limitations of the camera result in acquisition only of the frame before failure and the frame after failure. Without high-speed image capturing, one is unable to observe the crack propagation events throughout the entire failure event. It is quite feasible that the secondary crack initiated prior to catastrophic failure but did not propagate through the sample because the initial crack alleviated the stress first. It is suspected that mechanically loading at elevated temperature promotes a more uniform tensile stress condition whereupon multiple failure sites can become active. The DIC maps clearly highlight the stress concentrations at such multiple sites in these thermomechanically loaded films, Fig. 7(d) and (i). The secondary crack initiation site is linked to areas undergoing high tensile and high compressive stresses in close proximity. In the room temperature deposits, such paired sites do not appear to form which may explain the difference in behavior between the deposits.

Comparatively, the primary fracture in the ternary Ni-40Cu-0.6P alloy transmits through the small nick on the bottom right side of the film, marked by the black arrow in Fig. 7(i), while the secondary fracture initiates from the lighter contrast region on the left side of the film. These features are also highlighted in the corresponding DIC maps by the compressive (purple) spots marked with thick black arrows. The existence of compressive strains within this specimen could be unintuitive since the sample is tested in tension. Noticeably, the areas

adjacent to the compressive strain are undergoing significant tensile strain as compared to the rest of the foil. This appears to induce a compressive load on the neighboring grains in accommodating the overall deformation. This result highlights one of the benefits of DIC as a useful characterization method for evaluation of the deformation behavior in NC alloys. Ultimately, the secondary fracture terminates in an area with a refined grain size (compared to larger grains on the edges of the foils), in a region under tensile strain (red) shown in Fig. 7(i,j).

In this thermomechanically loaded state, the DIC maps reveal competition between multiple sites for failure, Fig. 7(d,i), regardless of composition. This results in two cracks which both propagate through the specimens at nearly the same time. In both deposits, the secondary fracture terminates in a region under tensile strain and at a refined local grain size compared to the edges of the foils. The DIC maps suggest that the secondary fracture may alleviate a small, localized strain while the primary fracture alleviates a larger strain nearby.

Like the specimens loaded at RT, the strain values reported by the DIC maps vary from the far-field strain measured across the shuttle. The far-field strain measured across the entirety of these specimens, Fig. 2(c, d), varies from the maximum strain measured here as expected. The binary Ni-40Cu alloy is measured to achieve a maximum strain of ≈ 2.4 % and the ternary alloy is measured to achieve a maximum strain of ≈ 5.7 % for the entire test to failure. The DIC map of the binary alloy, again only analyzing the last 60 s. before failure, shows a maximum local strain value of ≈ 7.4 %, Fig. 7(d), and a calculated far-field strain measurement of 0.70 % ± 0.05 % which differs slightly from the manual far-field strain measurement of ≈ 0.96 % over the same time frame. Similarly, the ternary alloy is reported to achieve a maximum of ≈ 4.5 % local strain by DIC during the last 60 s. of loading, Fig. 7(i), and a calculated far-field strain of 0.64 % ± 0.05 % which compares to the manual far-field strain measurement of ≈ 1.16 % for this frame range.

The far-field strain measurements calculated by DIC are generally lower than those measured by hand. This variation can be attributed to the specimen noticeably slipping from the grips near the end of the test as mentioned above in Section 3.1. The slippage would increase the strain value reported by manual measurement across the gap as compared to the DIC measurement reported here. Overall, the variation between the DIC-calculated far-field strain values and manually measured strain values are not substantially large and give confidence in the application of DIC to polycrystalline materials as reported.

High magnification micrographs of the primary fracture line confirm intergranular fracture behavior, Fig. 8. Like the RT sample, upon annealing and loading the Ni-40Cu alloy, the grains have a jagged profile but with significantly less light contrast grains from the grains tearing and sliding part, Fig. 8(a). This could be tied to the annealing process sealing fissures within the structure, resulting in less shearing within the plane of the film. The Ni-40Cu-0.6P alloy continued to display the jagged, fine-toothed fracture surface, Fig. 8(b), which is linked to the strengthening of the GBs by P as discussed above.

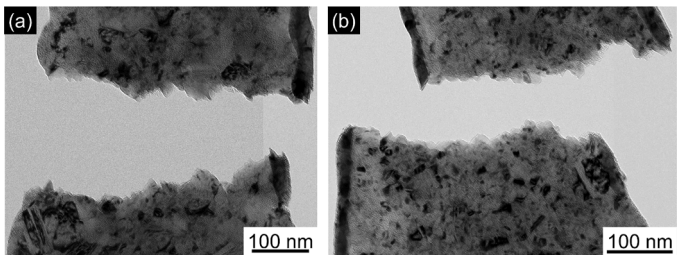

Fig. 8. High magnification brightfield micrographs stitched together **(a)** the fracture surface of Ni-40Cu upon thermomechanically loading at 150 °C and **(b)** the fracture surface of Ni-40Cu-0.6P upon thermomechanically loading at 150 °C.

3.2.4. High temperature modeling

The failure surface of the Ni-40Cu and Ni-40Cu-0.6P alloy at 150 °C, Fig. 8, is consistent with those results demonstrated at room temperature. Atomistic modeling of the 8 nm structures at 150 °C, Fig. 9(a), under isothermal-isovolumetric (canonical ensemble) conditions reveals enhanced ductility at elevated temperatures for both compositions. Interestingly, the elemental Ni structure deviates dramatically in its strength and ductility at 150 °C compared to RT while the Ni-1P alloy displays only a slight difference. Furthermore, calculation of the yield strength for the Ni and Ni-1P alloys using the 0.2 % offset method [77] suggests that the yield strength of pure Ni is similar to its strength at room temperature while Ni-1P declines slightly. Nevertheless, Ni-1P has a higher yield strength than pure Ni regardless of the temperature studied, Table 1.

The modeled, idealized Ni structure appears to gain strength at 150 °C which contrasts with the experimental results. Furthermore, the elemental Ni structure also exhibits a much more substantial drop in strength during failure which is indicative that cracks propagate even more effectively through Ni at higher temperature than at RT. The discrepancy between the experimentally observed drop in strength at elevated temperature is tied to the difference between the idealized modeled structure (which has no pre-existing flaws) and the nano-cracks that are present in the experimental structure as has been reported for Ni previously [95].

The higher yield strength of Ni-1P system stems from the fact that the segregation of P atoms strengthens the GBs, evident from the works in reference [10]. Appendix Fig. A7 shows the percentage of total strain accommodation in different mechanisms, as a function of applied strain at 23 °C. It can be seen from this plot that the contribution of GB mechanisms towards strain accommodation is higher in NC Ni than in Ni-1P, demonstrating the expected GB strengthening from the interfacial solute segregation in the Ni-P system. While an increase of temperature has a softening effect on strength, it is much more pronounced in Ni-1P system than pure Ni, as GBs are already weaker in the latter.

Examination of the microstructures as they fail, Fig. 9(b,c), shows a similar trend as observed at RT. In the elemental Ni structure, two cracks nucleate at a strain value of 14.55 % and rapidly grow across the next 0.1 % of strain. The proximity of these simultaneous initiation sites likely contributes to the significant increase in magnitude of the strength lost during failure shown in Fig. 9(a). Comparatively, the Ni-1P alloy nucleates one crack at a strain value of 7.6 %, nucleates a secondary crack at 7.65 % strain on the opposite side of the structure, wherein the two cracks slowly grow towards each other over the next 0.35 % strain. These results highlight the significance of the crack number density and distribution. Ultimately what dictates the failure behavior of the experimental films may be the proposed nanoscale cracks, their number density, and distribution through the film structures.

Consideration of this crack propagation behavior implies that the modeling results are consistent with the experimental findings, as the Ni-40Cu deposit fails at a much lower stress when thermomechanically loaded at 150 °C, while the Ni-40Cu-0.6P deposit exhibits a less significant drop in ultimate tensile strength (UTS) upon subjecting it to a thermomechanical load state. The Ni-40Cu specimen is very well-behaved in its agreement with the model suggesting that if a crack preexists within the foil, the foil should fail much faster at elevated temperatures than at room temperature. While the Ni-40Cu-0.6P alloy does not behave as well as the binary system in that the difference in UTS is more apparent experimentally than the model would predict. Collctively, there may well be differences in the crack density between the RT and 150 °C loaded structures which are not obvious via BF-TEM.

4. Collective conclusions and outlook

In situ RT loading of nanocrystalline Ni-40Cu and Ni-40Cu-0.6P reveals similar fracture strength which aligns with their similar grain size and the homogenous distribution of P in the ternary alloy. Nevertheless,

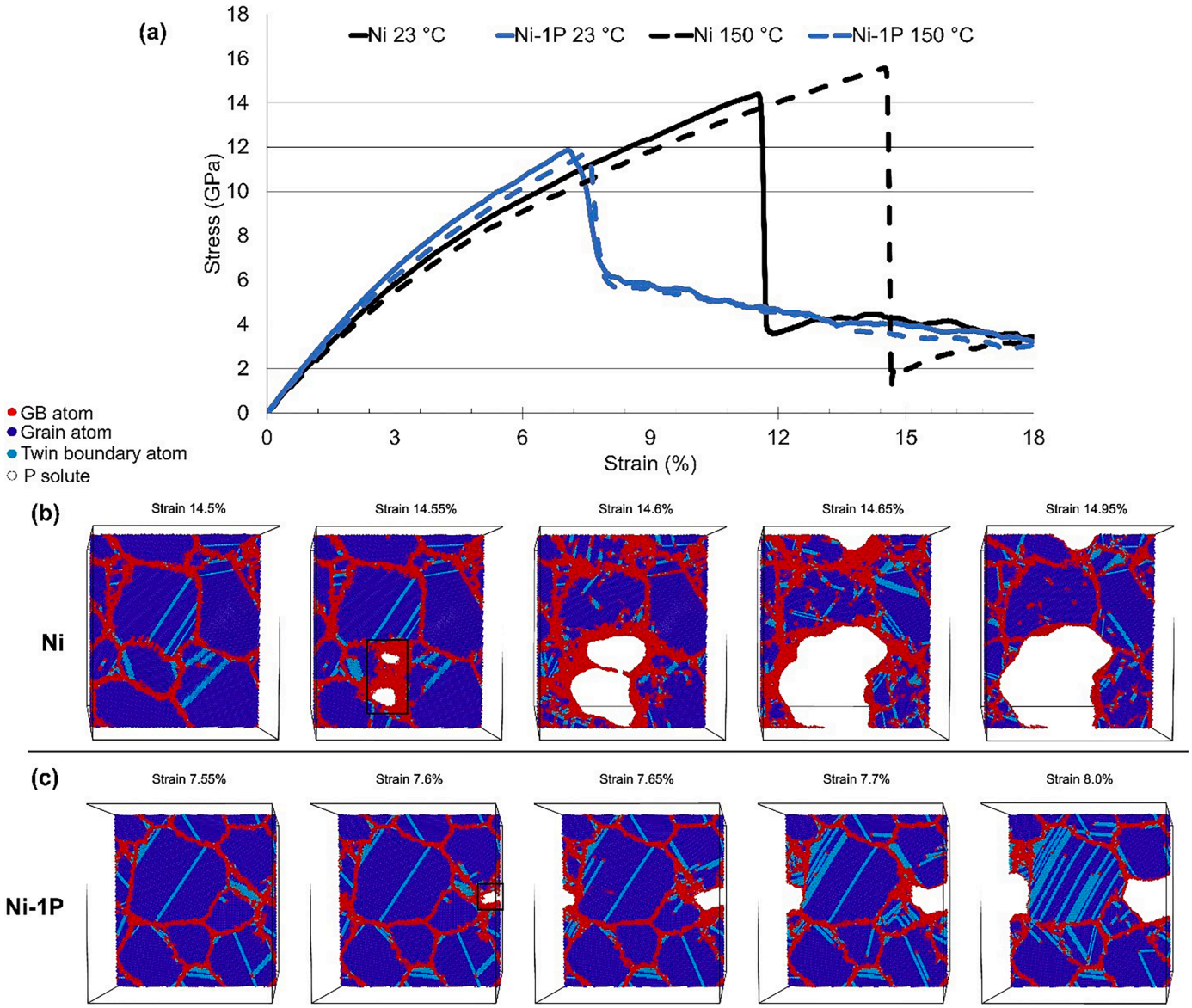

Fig. 9. (a) A stress-strain plot showing the failure behavior of Ni and Ni-1P with an 8 nm grain size under isothermal-isovolumetric load at 150 °C. Beneath are 2D slices through **(b)** the elemental Ni structure as it fails at 150 °C, and **(c)** the Ni-1P structure as it fails at 150 °C. Black boxes enclose the nucleation site of the crack in the first frame that the crack has formed. (For interpretation of the references to color in this figure legend, the reader is referred to the web version of this article.)

Table 1
Yield strengths of Ni-1P and Ni systems at different temperatures, as obtained by the 0.2 % offset method from the stress-strain curves provided in Fig. 9a.

Temperature	23 °C		150 °C	
System	**Ni-1P**	**Ni**	**Ni-1P**	**Ni**
Yield strength (GPa)	4.9	4.1	4.6	4.1

there are variations in crack formation and fracture surface profile, with the slight amount of P solute strengthening the GBs. The difference in crack behavior is confirmed through atomistic simulations of deformation flow stress.

The alloys soften when thermomechanically loaded at 150 °C, irrespective of composition, but a substantially higher fraction of its strength is retained in the ternary alloy over the binary regardless of loading temperature. This is attributed to the Ni-40Cu maintaining a slightly coarser grain size than the Ni-40Cu-0.6P and the P providing additional GB strength.

DIC mapping is shown to aid in evaluating regions of interest and map well to where ultimate failure points initiate. The calculated far-field strain values extracted from DIC and those from manual far-field strain measurements, over the same analysis period, show reasonably good agreement. Any such differnces are attributed to the inherent limitations and errors in each measurement. For example, DIC is susceptible for aberrations in contrast changes from Bragg and the far-field in specimen alignment and security of weld joints (which were more susceptible to loosening with temperature) to name a few. Regardless of these issues, the values reported are of the correct order of magnitude for mechanical testing of thin films. The application of DIC as a data-mining tool is shown to be a technological advancement that can aid in identifying significant events in the microstructural response to external stimuli.

Intergranular failure was prevalent in both samples at both temperature loading conditions. At RT, the Ni-40Cu film reveal more sliding and tearing apart of the film as compared to the Ni-40Cu-0.6P For the ternary alloy, a jagged, fine tooth failure surface is seen and linked to the P strengthening the boundaries.

Modeling of the fracture behavior of 8 nm grain size Ni and Ni-1P, for

comparison to the experimentally probed alloys, reveal that the addition of P promoted an increase in flow stress and distributed a higher fraction of the strain to the GBs under isothermal-isobaric conditions. Furthermore, under isothermal-isovolumetric conditions, it was found that the elemental Ni structure fail more rapidly after crack nucleation than Ni-1P Visualization of the model structures support the experimental findings wherein the P-enriched alloy exhibits a finer tooth fracture edge upon failing than the Ni-40Cu alloy. The model results were within error at RT and consistent with the experimental results at 150 °C, with the latter revealing the significance of crack number density and distribution on the ultimate tensile strength of the system.

CRediT authorship contribution statement

TRK performed the experiments, conducted the data analysis, and provided the first draft. HW designed the devices used and provided the electro-thermomechanical models for temperature calibration. AG provided atomistic simulations to supplement the experimental findings. YZ guided the device design and modeling to fit within the experimental restrictions. GT and GBT conceived the research objectives, assisted in data interpretation and context, and editing of the paper. The authors declare that they have no known competing financial interests or personal relationships that could have appeared to influence the work reported in this paper.

Declaration of Competing Interest

The authors declare that they have no known competing financial interests or personal relationships that could have appeared to influence the work reported in this paper.

Acknowledgments

The authors gratefully acknowledge the support of the Army Research Office grant W911NF-17-1-0528, Dr. Michael Bakas, program manager. The Alabama Analytical Research Center (AARC) at the University of Alabama is acknowledged for use of SEM-FIB and TEM. HW and YZ acknowledges the support of the National Science Foundation (awards no. 1762511 and 1929646). TRK also acknowledges Kayla Cole-Piepke at the University of Alabama for LabView code required to run the source meter units in the MEMS chip.

Supplementary materials

Supplementary material associated with this article can be found, in the online version, at doi:10.1016/j.actamat.2023.119462.

Appendix A1. – MEMS Device Operation

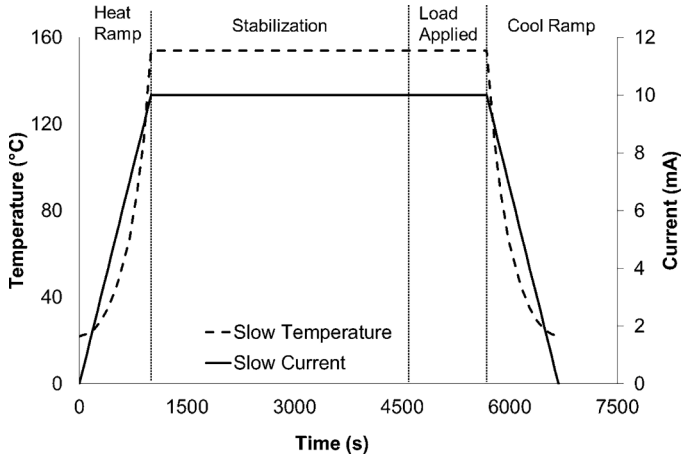

Fig. A1. The annealing treatment applied to the specimens reported herein. Temperature was ramped via a current of 0.01 mA·s^{-1} which was held for 1 h before a mechanical load was applied.

For the thermomechanical conditions, the specimens were annealed *in situ* to partition the P solute to the boundaries and then loaded. A representative curve showing this sequence is given in Fig. A1. For the force measurements during testing, the applied force for a specimen is obtained by comparing the "gap" distance with and without the specimen mounted under the same actuation force. For the electrostatic actuator, the actuation force is proportional to the square of the actuation voltage (Va^2). A lumped mechanical model of the device is given below, Fig. A2. The device consists of two shuttles (A, B) with a "gap" in between, where the specimen is mounted. The supporting beams of the two shuttles have the same stiffness *k*.

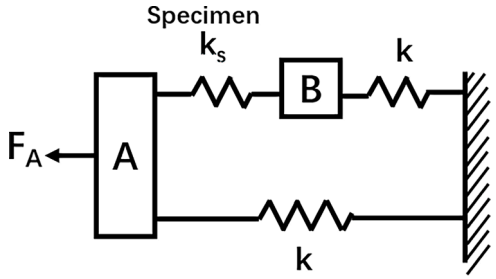

Fig. A2. A spring block diagram representative of the MEMS device system used for thermomechanically loading specimens in this work.

The device without specimen:

$$x_0 = \frac{F_A}{k} \tag{A1}$$

$$g_0 = x_0 + g_i \tag{A2}$$

The device with specimen:

$$kx_A + k_s x_s = F_A \tag{A3}$$

$$k_s x_s = kx_B \tag{A4}$$

$$x_A = x_s + x_B \tag{A5}$$

$$g = x_s + g_i \tag{A6}$$

Combining these six equations can give the force on the specimen (F_s) as

$$F_s = \frac{k}{2}(g_0 - g) \tag{A7}$$

where F_A is actuation force, x_0 is displacement of shuttle A without specimen, $k$and k_s is stiffness of Z-beam and specimen, x_A, x_B and x_s are displacement of shuttle A, B and specimen, g_i is the initial "gap" distance without specimen and actuation voltage, g_0 is the "gap" distance without the specimen under actuation voltage, and g is the "gap" distance with the specimen under the same actuation voltage.

According to this equation, when the stiffness k of the supporting beams of the shuttle is known, and the "gap" distances with and without specimen under the same actuation voltage are known, one can calculate the force in the specimen, from which the stress can be calculated. The stiffness k can be calculated using finite element simulation with the well-characterized dimensions of the supporting beams. The simulated stiffnesses for the three devices are 204 ± 7 N/m at room temperature or 191.7 N/m at 150 °C. The "gap" distances without a specimen at different actuation voltages are obtained during calibration of the device. The "gap" distances with a specimen are obtained during the testing and measured in post-processing.

Herein, the device has been carefully designed, including the dimensions of the Z-beams, to obtain appropriate stiffness, such that the specimen can be substantially deformed without pulling the load sensor too much. As an example, for a specimen with length of 1 μm, thickness of 500 nm, width of 75 nm, and Young's modulus of 2 GPa, the stiffness of the specimen is calculated to be 75 N/m based on EA/L. This value is smaller than the stiffness of the Z-beam (204 N/m) in the experimental setup.

Specimen unfurling and slippage are experimental realities despite the best efforts to minimize their effects. During the lift-out process, some foils will be placed on the device in a highly relaxed "furled" state, Fig. A3. A tensile load applied will then unfurl the foils to the point of being taut wherein the microstructure then begins to accommodate the load. Additionally, specimens may undergo slippage and pull out from the Pt grips at higher loads which manifests itself in higher strain rates at high loads. This is much more difficult to consistently verify in the data by eye and has not been subtracted from our data sets to ensure consistency between them.

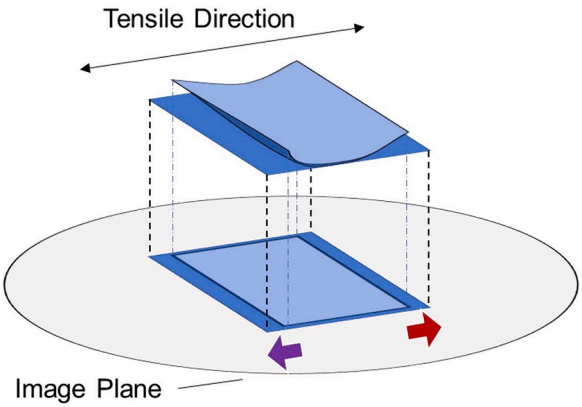

Fig. A3. A furled specimen (light blue) would appear to deform substantially upon initial loading of the device (dark blue). (For interpretation of the references to color in this figure legend, the reader is referred to the web version of this article.)

In the Ni-40Cu alloy loaded at 150 °C, a substantial increase in strain is noted between the first two data points, signifying such a relaxed state in the film was present as it was prepared for load testing. There are two implications of this at elevated temperatures. First, that the specimen is unfurling when a mechanical stimulus is being applied indicating the thermal expansion of the shuttle when heating to 150 °C is effectively applying a net load and strain of near-zero on the structure since the specimen is unfurling in response to the thermal expansion. As such, the thermal stress and strain components are taken to be zero in the real data. Additionally, one notes that the stress corresponding to the measured strain is exceptionally small, per equation 7 above, as the device itself provides most of the resistance to the load. Assuming an elastic response in this early stage of loading, one can use a linear slope to calculate the stress-strain relationship at this low stress value and therein extrapolate the corresponding true strain value (0.05 % in this case) from the system. The difference between the measured strain and this true strain value (2.2 % in this case) is then subtracted from the subsequent data points while the first non-zero data point is set equal to the calculated true strain value. Comparison of Appendix Fig. A4(e) with Fig. 2(e) in the text shows the difference between the corrected and uncorrected data sets.

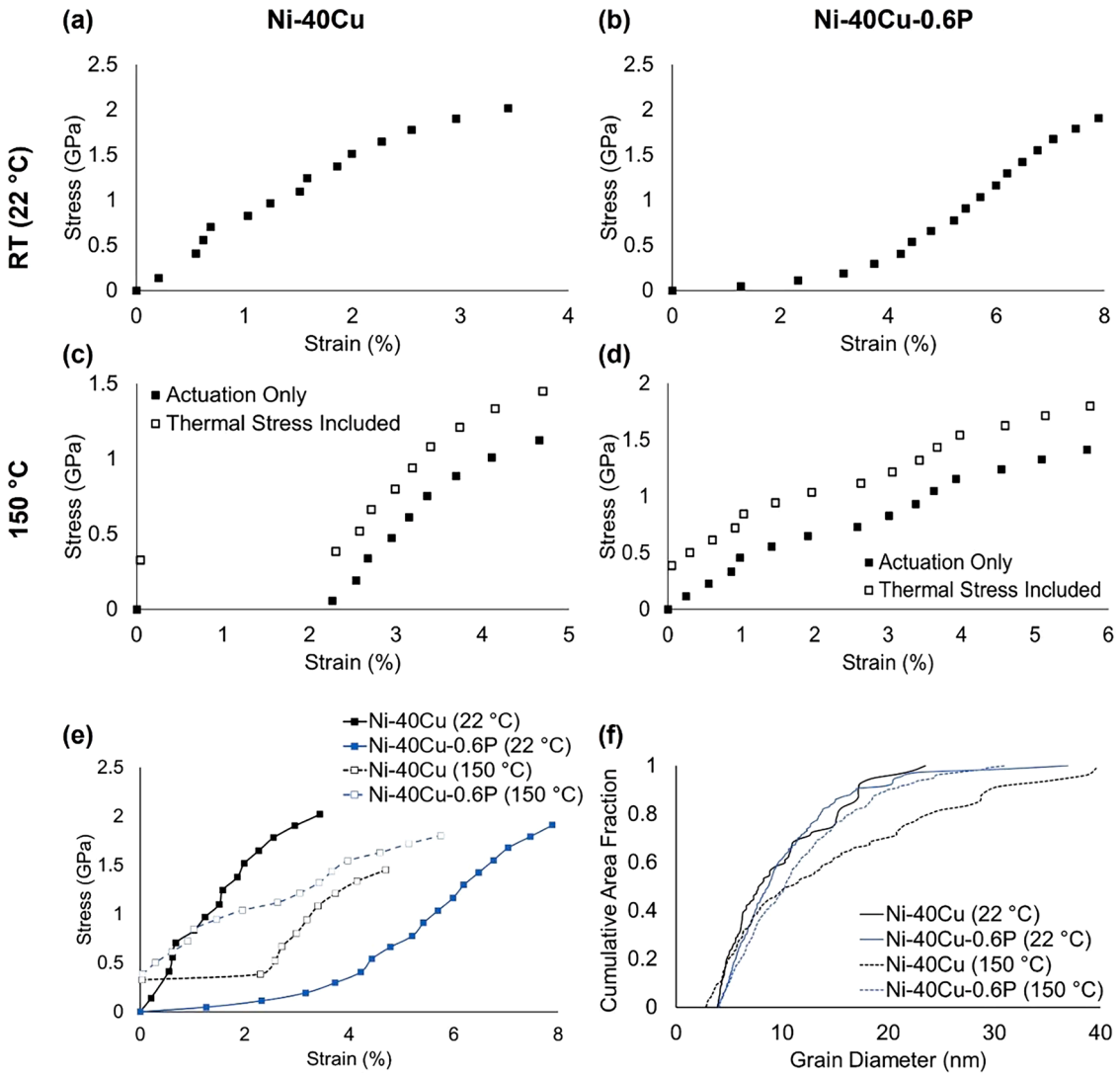

Fig. A4. Mechanical and microstructural properties measured during testing of the NC foils. Stress-strain and force-time plot of **(a)** Ni-40Cu at RT; **(b)** Ni-40Cu-0.6P at RT; **(c)** Ni-40Cu at 150 °C; **(d)** Ni-40Cu-0.6P at 150 °C. Cumulative plots for all specimens: **(e)** raw stress-strain curves for all conditions; **(f)** initial grain size distributions measured by dark field techniques. (For interpretation of the references to color in this figure legend, the reader is referred to the web version of this article.)

Appendix A2 – Shear Strain DIC Maps

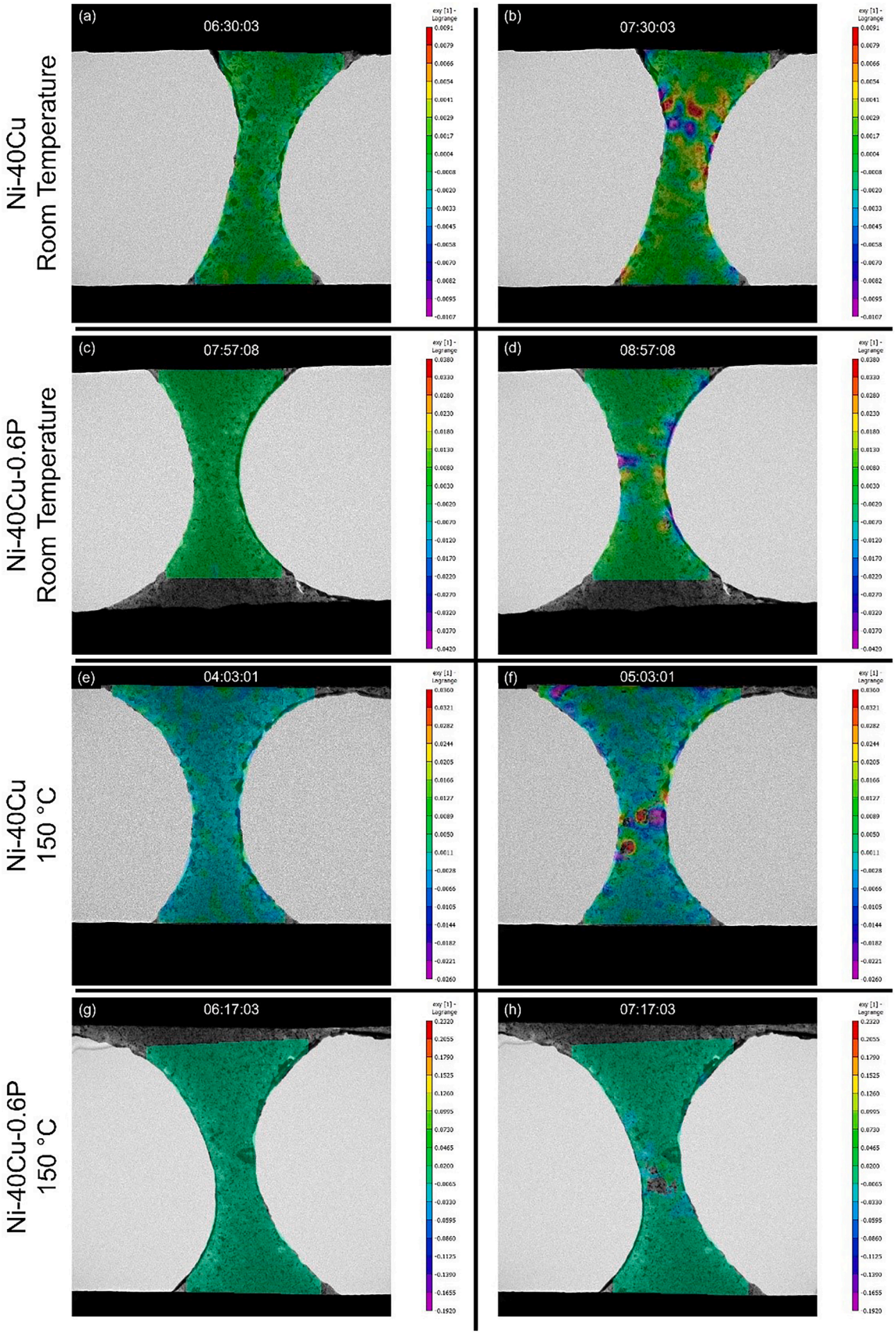

Fig. A5. DIC maps displaying the shear strain component, exy. **(a)** reference frame of Ni-40Cu at RT, **(b)** Ni-40Cu at RT, just before failure, **(c)** reference frame of Ni-40Cu-0.6P at RT, **(d)** Ni-40Cu-0.6P at RT, just before failure, **(e)** reference frame of Ni-40Cu at 150 °C, **(f)** Ni-40Cu at 150 °C, just before failure, **(g)** reference frame of Ni-40Cu-0.6P at 150 °C, **(h)** Ni-40Cu-0.6P at 150 °C, just before failure. (For interpretation of the references to color in this figure legend, the reader is referred to the web version of this article.)

Appendix A3 – Highlighting Nanoscale Cracks in the As-Deposited Condition

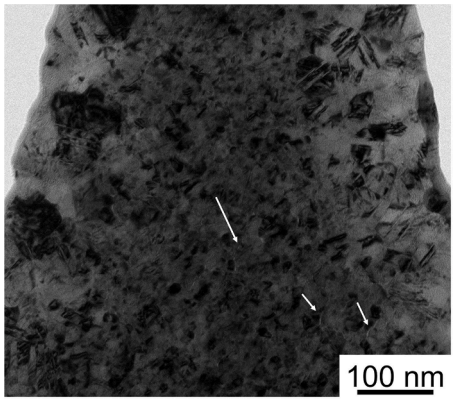

Fig. A6. Brightfield micrograph of Ni-40Cu as-deposited, prior to loading or heating. White arrows guide the eye to nanoscale cracks within the structure in the as-deposited state.

Appendix A4 – Strain Accommodation Mechanisms in Nanocrystalline Ni and Ni-1P

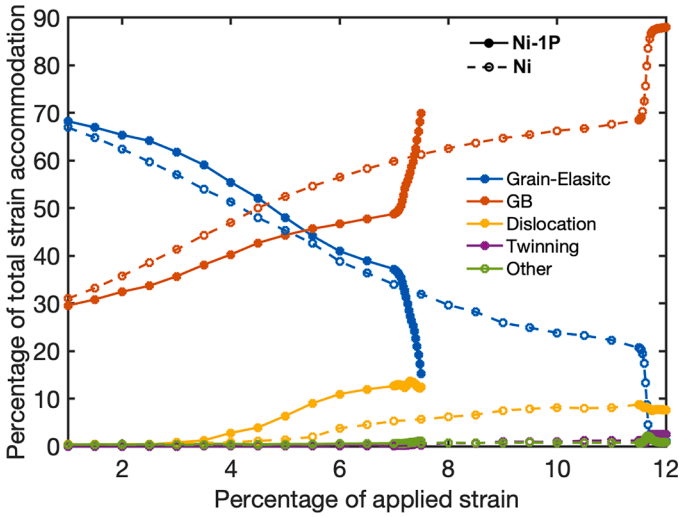

Fig. A7. Percentages of total strain accommodation by individual deformation mechanisms during the uniaxial tensile loading of NC Ni-1P (solid lines) and Ni (dashed lines) structures at 23 °C and in isothermal-isovolumetric (canonical) ensemble. (For interpretation of the references to color in this figure legend, the reader is referred to the web version of this article.)

References

[1] J. Weissmuller, Alloy effects in nanostructures, Nanostruct. Mater. 3 (1993) 261–272.
[2] T. Chookajorn, H.A. Murdoch, C.A. Schuh, Design of stable nanocrystalline alloys, Science 337 (2012) 951–954, https://doi.org/10.1126/science.1224737.
[3] R.K. Koju, K.A. Darling, K.N. Solanki, Y. Mishin, Atomistic modeling of capillary-driven grain boundary motion in Cu-Ta alloys, Acta Mater. 148 (2018) 311–319, https://doi.org/10.1016/j.actamat.2018.01.027.
[4] R.O. Scattergood, C.C. Koch, A modified model for hall-petch behavior in nanocrystalline materials, Scr. Metall. Mater. 27 (1992) 1195–1200, https://doi.org/10.1016/0956-716X(92)90598-9.
[5] T. Chookajorn, M. Park, C.A. Schuh, Duplex nanocrystalline alloys: entropic nanostructure stabilization and a case study on W–Cr, J. Mater. Res. 30 (2015) 151–163, https://doi.org/10.1557/jmr.2014.385.
[6] A.R. Kalidindi, C.A. Schuh, Stability criteria for nanocrystalline alloys, Acta Mater. 132 (2017) 128–137, https://doi.org/10.1016/j.actamat.2017.03.029.
[7] H.A. Murdoch, C.A. Schuh, Estimation of grain boundary segregation enthalpy and its role in stable nanocrystalline alloy design, J. Mater. Res. 28 (2013) 2154–2163, https://doi.org/10.1557/jmr.2013.211.
[8] J.R. Trelewicz, C.A. Schuh, Grain boundary segregation and thermodynamically stable binary nanocrystalline alloys, Phys. Rev. B. 79 (2009), 094112, https://doi.org/10.1103/PhysRevB.79.094112.
[9] K.A. Darling, M.A. Tschopp, B.K. VanLeeuwen, M.A. Atwater, Z.K. Liu, Mitigating grain growth in binary nanocrystalline alloys through solute selection based on thermodynamic stability maps, Comput. Mater. Sci. 84 (2014) 255–266, https://doi.org/10.1016/j.commatsci.2013.10.018.
[10] A. Gupta, J. Gruber, S.S. Rajaram, G.B. Thompson, D.L. McDowell, G.J. Tucker, On the mechanistic origins of maximum strength in nanocrystalline metals, NPJ Comput. Mater. 6 (2020) 153, https://doi.org/10.1038/s41524-020-00425-0.
[11] X. Zhou, A. Gupta, G.J. Tucker, G.B. Thompson, Manipulation of solute partitioning mechanisms for nanocrystalline stability, Acta Mater. 208 (2021), 116662, https://doi.org/10.1016/j.actamat.2021.116662.
[12] I. Matsui, Y. Takigawa, T. Uesugi, K. Higashi, Tensile properties of bulk nanocrystalline Ni and Ni-W fabricated by sulfamate bath, MSF 654–656 (2010) 1114–1117, https://doi.org/10.4028/www.scientific.net/MSF.654-656.1114.
[13] C. Gu, J. Lian, Z. Jiang, Q. Jiang, Enhanced tensile ductility in an electrodeposited nanocrystalline Ni, in: 2006 IEEE Conference on Emerging Technologies - Nanoelectronics, IEEE, Singapore, 2006, pp. 293–297, https://doi.org/10.1109/NANOEL.2006.1609732.
[14] X. Zhou, X. Yu, T. Kaub, R.L. Martens, G.B. Thompson, Grain boundary specific segregation in nanocrystalline Fe(Cr), Sci. Rep. 6 (2016) 34642, https://doi.org/10.1038/srep34642.
[15] R. Kirchheim, Grain coarsening inhibited by solute segregation, Acta Mater. 50 (2002) 413–419, https://doi.org/10.1016/S1359-6454(01)00338-X.
[16] X. Zhou, R. Darvishi Kamachali, B.L. Boyce, B.G. Clark, D. Raabe, G.B. Thompson, Spinodal Decomposition in Nanocrystalline Alloys, Acta Mater. 215 (2021), 117054, https://doi.org/10.1016/j.actamat.2021.117054.

[17] E. Hosseinian, O.N. Pierron, Quantitative in situ TEM tensile fatigue testing on nanocrystalline metallic ultrathin films, Nanoscale 5 (2013) 12532–12541, https://doi.org/10.1039/C3NR04035F.

[18] S. Gupta, O.N. Pierron, A MEMS Tensile Testing Technique for Measuring True Activation Volume and Effective Stress in Nanocrystalline Ultrathin Microbeams, J. Microelectromech. Syst. 26 (2017) 1082–1092, https://doi.org/10.1109/JMEMS.2017.2708522.

[19] P. Choi, M. Dasilva, U. Klement, T. Alkassab, R. Kirchheim, Thermal stability of electrodeposited nanocrystalline Co-1.1at.%P, Acta Mater. 53 (2005) 4473–4481, https://doi.org/10.1016/j.actamat.2005.06.006.

[20] E.O. Hall, The deformation and ageing of mild steel: iii discussion of results, Proc. Phys. Soc. B. 64 (1951) 747–753, https://doi.org/10.1088/0370-1301/64/9/303.

[21] N.J. Petch, The cleavage strength of polycrystals, J. Iron Steel Institute 174 (1953) 25–28.

[22] B.Chad Hornbuckle, C.L. Williams, S.W. Dean, X. Zhou, C. Kale, S.A. Turnage, J. D. Clayton, G.B. Thompson, A.K. Giri, K.N. Solanki, K.A. Darling, Stable microstructure in a nanocrystalline copper–tantalum alloy during shock loading, Commun. Mater. 1 (2020) 22, https://doi.org/10.1038/s43246-020-0024-3.

[23] J.G. Brons, G.B. Thompson, Abnormalities associated with grain growth in solid solution Cu(Ni) thin films, Thin Solid Films 558 (2014) 170–175, https://doi.org/10.1016/j.tsf.2014.03.009.

[24] J.G. Brons, G.B. Thompson, A comparison of grain boundary evolution during grain growth in fcc metals, Acta Mater. 61 (2013) 3936–3944, https://doi.org/10.1016/j.actamat.2013.02.057.

[25] K. Kruska, A. Rohatgi, R.S. Vemuri, L. Kovarik, T.H. Moser, J.E. Evans, N. D. Browning, Grain Growth in Nanocrystalline Mg-Al Thin Films, Metall. Mater. Trans. A 48 (2017) 6118–6125, https://doi.org/10.1007/s11661-017-4350-0.

[26] Y. Zhang, G.J. Tucker, J.R. Trelewicz, Stress-assisted grain growth in nanocrystalline metals: grain boundary mediated mechanisms and stabilization through alloying, Acta Mater. 131 (2017) 39–47, https://doi.org/10.1016/j.actamat.2017.03.060.

[27] D.S. Gianola, S. Van Petegem, M. Legros, S. Brandstetter, H. Van Swygenhoven, K. J. Hemker, Stress-assisted discontinuous grain growth and its effect on the deformation behavior of nanocrystalline aluminum thin films, Acta Mater. 54 (2006) 2253–2263, https://doi.org/10.1016/j.actamat.2006.01.023.

[28] S. Kumar, T. Alam, A. Haque, Quantitative in-situ TEM study of stress-assisted grain growth, MRS Commun. 3 (2013) 101–105, https://doi.org/10.1557/mrc.2013.15.

[29] S. Gollapudi, K.V. Rajulapati, I. Charit, C.C. Koch, R.O. Scattergood, K.L. Murty, Creep in nanocrystalline materials: role of stress assisted grain growth, Mater. Sci. Eng.: A 527 (2010) 5773–5781, https://doi.org/10.1016/j.msea.2010.05.048.

[30] Y. Zhang, J.A. Sharon, G.L. Hu, K.T. Ramesh, K.J. Hemker, Stress-driven grain growth in ultrafine grained Mg thin film, Scr. Mater. 68 (2013) 424–427, https://doi.org/10.1016/j.scriptamat.2012.11.013.

[31] G.S. Rohrer, Introduction to grains, phases, and interfaces—an interpretation of microstructure, Trans. AIME, 1948, vol. 175, pp. 15–51, by C.S. Smith, Metall. Materi. Trans. B 41 (2010) 457–494, https://doi.org/10.1007/s11663-010-9364-6.

[32] P.A. Manohar, M. Ferry, T. Chandra, Five decades of the zener equation, ISIJ Int. 38 (1998) 913–924, https://doi.org/10.2355/isijinternational.38.913.

[33] B.C. Hornbuckle, K. Solanki, K.A. Darling, Prolonged high-temperature exposure: tailoring nanocrystalline Cu–Ta alloys against grain growth, Mater. Sci. Eng.: A 824 (2021), 141818, https://doi.org/10.1016/j.msea.2021.141818.

[34] K.A. Darling, M. Rajagopalan, M. Komarasamy, M.A. Bhatia, B.C. Hornbuckle, R. S. Mishra, K.N. Solanki, Extreme creep resistance in a microstructurally stable nanocrystalline alloy, Nature 537 (2016) 378–381, https://doi.org/10.1038/nature19313.

[35] F. Liu, R. Kirchheim, Nano-scale grain growth inhibited by reducing grain boundary energy through solute segregation, J. Cryst. Growth 264 (2004) 385–391, https://doi.org/10.1016/j.jcrysgro.2003.12.021.

[36] M. Jin, A.M. Minor, J.W. Morris, Strain-induced coarsening in nano-grained films, Thin Solid Films 515 (2007) 3202–3207, https://doi.org/10.1016/j.tsf.2006.01.052.

[37] R.C. Hugo, H. Kung, J.R. Weertman, R. Mitra, J.A. Knapp, D.M. Follstaedt, In-situ TEM tensile testing of DC magnetron sputtered and pulsed laser deposited Ni thin films, Acta Mater. 51 (2003) 1937–1943, https://doi.org/10.1016/S1359-6454(02)00599-2.

[38] D. Oliveros, A. Fraczkiewicz, A. Dlouhy, C. Zhang, H. Song, S. Sandfeld, M. Legros, Orientation-related twinning and dislocation glide in a cantor high entropy alloy at room and cryogenic temperature studied by in situ TEM straining, Mater. Chem Phys. 272 (2021), 124955, https://doi.org/10.1016/j.matchemphys.2021.124955.

[39] Q. Guo, Y. Gu, C.M. Barr, T. Koenig, K. Hattar, L. LiG, G.B. Thompson, *In situ* indentation and high cycle tapping deformation responses in a nanolaminate crystalline/amorphous metal compositee Cu thin film, Mater. Sci. Eng.: A 798 (2020), 140074, https://doi.org/10.1016/j.msea.2020.140074.

[40] E. Lang, M. Marshall, H. Padilla, B. Boyce, K. Hattar, In-situ TEM cryoindentation of nanocrystalline copper, Microsc. Microanal. 27 (2021) 1492–1493. doi:10.1017/S1431927621005493.

[41] T.-H. Chang, Y. Zhu, A microelectromechanical system for thermomechanical testing of nanostructures, Appl. Phys. Lett. 103 (2013), 263114, https://doi.org/10.1063/1.4858962.

[42] C. Guan, Y. Zhu, An electrothermal microactuator with Z-shaped beams, J. Micromech. Microeng. 20 (2010), 085014, https://doi.org/10.1088/0960-1317/20/8/085014.

[43] Y. Zhu, T.-H. Chang, A review of microelectromechanical systems for nanoscale mechanical characterization, J. Micromech. Microeng. 25 (2015), 093001, https://doi.org/10.1088/0960-1317/25/9/093001.

[44] Y. Zhu, H.D. Espinosa, An electromechanical material testing system for in situ electron microscopy and applications, Proc. Natl. Acad. Sci. 102 (2005) 14503–14508, https://doi.org/10.1073/pnas.0506544102.

[45] M.A. Haque, M.T.A. Saif, Deformation mechanisms in free-standing nanoscale thin films: a quantitative *in situ* transmission electron microscope study, Proc. Natl. Acad. Sci. U.S.A. 101 (2004) 6335–6340, https://doi.org/10.1073/pnas.0400066101.

[46] G. Cheng, Y. Zhu, In situ nano-thermo-mechanical experiment reveals brittle to ductile transition in Si nanowires, Microsc. Microanal. 26 (2020) 3192–3194, https://doi.org/10.1017/S1431927620024125.

[47] S. Gupta, A. Barrios, N. England, O.N. Pierron, Improved very high cycle bending fatigue behavior of Ni microbeams with Au coatings, Acta Mater. 161 (2018) 444–455, https://doi.org/10.1016/j.actamat.2018.09.037.

[48] S. Gupta, S. Stangebye, K. Jungjohann, B. Boyce, T. Zhu, J. Kacher, O.N. Pierron, *In situ* TEM measurement of activation volume in ultrafine grained gold, Nanoscale 12 (2020) 7146–7158, https://doi.org/10.1039/D0NR01874K.

[49] S. Kumar, X. Li, A. Haque, H. Gao, Is stress concentration relevant for nanocrystalline metals? Nano Lett. 11 (2011) 2510–2516, https://doi.org/10.1021/nl201083t.

[50] M.L. Taheri, T. Lagrange, B.W. Reed, M.R. Armstrong, G.H. Campbell, W. J. DeHope, J.S. Kim, W.E. King, D.J. Masiel, N.D. Browning, Laser-based in situ techniques: novel methods for generating extreme conditions in TEM samples, Microsc. Res. Tech. 72 (2009) 122–130, https://doi.org/10.1002/jemt.20664.

[51] P. Price, A. Cook, L. Treadwell, K. Hattar, Capabilities at Sandia National Laboratories, (n.d.) 24.

[52] K.S.N. Vikrant, R.L. Grosso, L. Feng, E.N.S. Muccillo, D.N.F. Muche, G. S. Jawaharram, C.M. Barr, A.M. Monterrosa, R.H.R. Castro, R.E. García, K. Hattar, S.J. Dillon, Ultrahigh temperature in situ transmission electron microscopy based bicrystal coble creep in zirconia I: nanowire growth and interfacial diffusivity, Acta Mater. 199 (2020) 530–541, https://doi.org/10.1016/j.actamat.2020.08.069.

[53] R.L. Grosso, K.S.N. Vikrant, L. Feng, E.N.S. Muccillo, D.N.F. Muche, G. S. Jawaharram, C.M. Barr, A.M. Monterrosa, R.H.R. Castro, R.E. García, K. Hattar, S.J. Dillon, Ultrahigh temperature in situ transmission electron microscopy based bicrystal coble creep in Zirconia II: interfacial thermodynamics and transport mechanisms, Acta Mater. 200 (2020) 1008–1021, https://doi.org/10.1016/j.actamat.2020.08.070.

[54] R.L. Grosso, E.N.S. Muccillo, D.N.F. Muche, G.S. Jawaharram, C.M. Barr, A. M. Monterrosa, R.H.R. Castro, K. Hattar, S.J. Dillon, In situ transmission electron microscopy for ultrahigh temperature mechanical testing of ZrO_2, Nano Lett. 20 (2020) 1041–1046, https://doi.org/10.1021/acs.nanolett.9b04205.

[55] G. Jawaharram, C. Barr, K. Hattar, S. Dillon, Evidence for a high temperature whisker growth mechanism active in tungsten during in situ nanopillar compression, Nanomaterials 11 (2021) 2429, https://doi.org/10.3390/nano11092429.

[56] G.S. Jawaharram, P.M. Price, C.M. Barr, K. Hattar, R.S. Averback, S.J. Dillon, High temperature irradiation induced creep in Ag nanopillars measured via in situ transmission electron microscopy, Scr. Mater. 148 (2018) 1–4, https://doi.org/10.1016/j.scriptamat.2018.01.007.

[57] F. Niekiel, S.M. Kraschewski, J. Müller, B. Butz, E. Spiecker, Local temperature measurement in TEM by parallel beam electron diffraction, Ultramicroscopy 176 (2017) 161–169, https://doi.org/10.1016/j.ultramic.2016.11.028.

[58] M. Mecklenburg, W.A. Hubbard, E.R. White, R. Dhall, S.B. Cronin, S. Aloni, B. C. Regan, Nanoscale temperature mapping in operating microelectronic devices, Science 347 (2015) 629–632, https://doi.org/10.1126/science.aaa2433.

[59] G. Cheng, Y. Zhang, T.-H. Chang, Q. Liu, L. Chen, W.D. Lu, T. Zhu, Y. Zhu, In situ nano-thermomechanical experiment reveals brittle to ductile transition in silicon nanowires, Nano Lett. 19 (2019) 5327–5334, https://doi.org/10.1021/acs.nanolett.9b01789.

[60] T.R. Koenig, I.B. Bikmukhametov, G.J. Tucker, G.B. Thompson, influence of ternary solute additions on nanocrystalline stability and mechanical behavior, Acta Mater. 239 (2022).

[61] W. Callister, Materials Science and Engineering: An Introduction, 7th ed., Wiley, 2006.

[62] I. Bikmukhametov, T.R. Koenig, G.J. Tucker, G.B. Thompson, A rapid preparation method for in situ nanomechanical TEM tensile specimens, J. Mater. Res. 36 (2021) 2315–2324, https://doi.org/10.1557/s43578-021-00167-9.

[63] M. Shamshirsaz, M.B. Asgari, Polysilicon micro beams buckling with temperature-dependent properties, Microsyst. Technol. 14 (2008) 957–961, https://doi.org/10.1007/s00542-008-0589-0.

[64] A. Cowen, G. Hames, D. Monk, S. Wilcenski, B. Hardy, SOIMUMPs Design Handbook, 2011.

[65] L.A. Giannuzzi, F.A. Stevie, A review of focused ion beam milling techniques for TEM specimen preparation, Micron 30 (1999) 197–204, https://doi.org/10.1016/S0968-4328(99)00005-0.

[66] M.K. Miller, K.F. Russell, G.B. Thompson, Strategies for fabricating atom probe specimens with a dual beam FIB, Ultramicroscopy 102 (2005) 287–298, https://doi.org/10.1016/j.ultramic.2004.10.011.

[67] J. Gruber, H. Lim, F. Abdeljawad, S. Foiles, G.J. Tucker, Development of physically based atomistic microstructures: the effect on the mechanical response of polycrystals, Comput. Mater. Sci. 128 (2017) 29–36, https://doi.org/10.1016/J.COMMATSCI.2016.07.011.

[68] A. Gupta, S.S. Rajaram, G.B. Thompson, G.J. Tucker, Improved computational method to generate properly equilibrated atomistic microstructures, MethodsX 8 (2021), 101217, https://doi.org/10.1016/j.mex.2021.101217.

[69] S. Plimpton, Fast parallel algorithms for short-range molecular dynamics, J. Comput. Phys. 117 (1995), https://doi.org/10.1006/jcph.1995.1039.

[70] A. Stukowski, Visualization and analysis of atomistic simulation data with OVITO-the Open Visualization Tool, Model. Simul. Mater. Sci. Eng. 18 (2010), https://doi.org/10.1088/0965-0393/18/1/015012.
[71] H. Okamoto, M.E. Schlesinger, E.M. Mueller (Eds.), Binary Alloy Phase Diagrams, in: Alloy Phase Diagrams, ASM International, 2016, https://doi.org/10.31399/asm.hb.v03.a0006247, 89–89.
[72] A. Gupta, X. Zhou, G.B. Thompson, G.J. Tucker, Role of grain boundary character and its evolution on interfacial solute segregation behavior in nanocrystalline Ni-P, Acta Mater. 190 (2020) 113–123, https://doi.org/10.1016/j.actamat.2020.03.012.
[73] H.W. Sheng, E. Ma, M.J. Kramer, Relating dynamic properties to atomic structure in metallic glasses, JOM (2012) 64, https://doi.org/10.1007/s11837-012-0360-y.
[74] S.M. Foiles, J.J. Hoyt, Computation of grain boundary stiffness and mobility from boundary fluctuations, Acta Mater 54 (2006) 3351–3357, https://doi.org/10.1016/J.ACTA- MAT.2006.03.037.
[75] G.J. Tucker, S. Tiwari, J.A. Zimmerman, D.L. McDowell, Investigating the deformation of nanocrystalline copper with microscale kinematic metrics and molecular dynamics, J. Mech. Phys. Solids 60 (2012) 471–486, https://doi.org/10.1016/J.JMPS.2011.11.007.
[76] G.J. Tucker, J.A. Zimmerman, D.L. McDowell, Continuum metrics for deformation and microrotation from atomistic simulations: application to grain boundaries, Int. J. Eng. Sci. 49 (2011) 1424–1434, https://doi.org/10.1016/J.IJENGSCI.2011.03.019.
[77] S.S. Rajaram, A. Gupta, G.B. Thompson, J. Gruber, A. Jablokow, G.J. Tucker, Grain-size-dependent grain boundary deformation during yielding in nanocrystalline materials using atomistic simulations, JOM 72 (2020), https://doi.org/10.1007/s11837-020-04036-4.
[78] I. Bikmukhametov, A. Gupta, T.R. Koenig, G.J. Tucker, G.B. Thompson, Consequences of solute partitioning on hardness in stabilized nanocrystalline alloys, Mater. Sci. Eng.: A 875 (2023), 145113, https://doi.org/10.1016/j.msea.2023.145113.
[79] D. Kiener, C. Motz, M. Rester, M. Jenko, G. Dehm, FIB damage of Cu and possible consequences for miniaturized mechanical tests, Mater. Sci. Eng.: A 459 (2007) 262–272, https://doi.org/10.1016/j.msea.2007.01.046.
[80] International Digital Image Correlation Society, E. Jones, M. Iadicola, R. Bigger, B. Blaysat, C. Boo, M. Grewer, J. Hu, A. Jones, M. Klein, K. Raghavan, P. Reu, T. Schmidt, T. Siebert, M. Simenson, D. Turner, A. Vieira, T. Weikert, A Good Practices Guide for Digital Image Correlation, International Digital Image Correlation Society, 2018, https://doi.org/10.32720/idics/gpg.ed1, 1st ed.
[81] W. Tong, An evaluation of digital image correlation criteria for strain mapping applications, Strain 41 (2005) 167–175, https://doi.org/10.1111/j.1475-1305.2005.00227.x.
[82] D. Adams, S. Irfan, J. Cramer, M.P. Miles, E.R. Homer, T. Brown, R.K. Mishra, D. T. Fullwood, Digital image correlation of forescatter detector images for simultaneous strain and orientation mapping, Microsc. Microanal. 26 (2020) 641–652, https://doi.org/10.1017/S1431927620001701.
[83] O. Glushko, A simple and effective way to evaluate the accuracy of digital image correlation combined with scanning electron microscopy (SEM-DIC), Results Mater. 14 (2022), 100276, https://doi.org/10.1016/j.rinma.2022.100276.
[84] A.D. Kammers, S. Daly, Digital image correlation under scanning electron microscopy: methodology and validation, Exp. Mech. 53 (2013) 1743–1761, https://doi.org/10.1007/s11340-013-9782-x.
[85] C.B. Montgomery, B. Koohbor, N.R. Sottos, A robust patterning technique for electron microscopy-based digital image correlation at sub-micron resolutions, Exp. Mech. 59 (2019) 1063–1073, https://doi.org/10.1007/s11340-019-00487-2.
[86] J.C. Stinville, T. Francis, A.T. Polonsky, C.J. Torbet, M.A. Charpagne, Z. Chen, G. H. Balbus, F. Bourdin, V. Valle, P.G. Callahan, M.P. Echlin, T.M. Pollock, Time-resolved digital image correlation in the scanning electron microscope for analysis of time-dependent mechanisms, Exp. Mech. 61 (2021) 331–348, https://doi.org/10.1007/s11340-020-00632-2.
[87] X. Wang, Z. Pan, F. Fan, J. Wang, Y. Liu, S.X. Mao, T. Zhu, S. Xia, Nanoscale deformation analysis with high-resolution transmission electron microscopy and digital image correlation, J. Appl. Mech. 82 (2015), 121001, https://doi.org/10.1115/1.4031332.
[88] Y. Zhang, L. Feng, S. Dillon, J. Lambros, Full-field deformation measurements in the transmission electron microscope using digital image correlation and particle tracking, Mater. Charact. 183 (2022), 111598, https://doi.org/10.1016/j.matchar.2021.111598.
[89] N. Lu, Z. Suo, J.J. Vlassak, The effect of film thickness on the failure strain of polymer-supported metal films, Acta Mater. 58 (2010) 1679–1687, https://doi.org/10.1016/j.actamat.2009.11.010.
[90] Y. Xiang, X. Chen, J.J. Vlassak, Plane-strain bulge test for thin films, J. Mater. Res. 20 (2005) 2360–2370, https://doi.org/10.1557/jmr.2005.0313.
[91] Y. Xiang, T. Li, Z. Suo, J.J. Vlassak, High ductility of a metal film adherent on a polymer substrate, Appl. Phys. Lett. 87 (2005), 161910, https://doi.org/10.1063/1.2108110.
[92] H. Okamoto, Ni-P (Nickel-Phosphorus), J. Phase Equilib. Diffus 31 (2010) 200–201, https://doi.org/10.1007/s11669-010-9664-1.
[93] H. Okamoto, Comment on Cu-P (copper-phosphorus), JPE 16 (1995) 368–369, https://doi.org/10.1007/BF02645303.
[94] A. Jain, S.P. Ong, G. Hautier, W. Chen, W.D. Richards, S. Dacek, S. Cholia, D. Gunter, D. Skinner, G. Ceder, K.A. Persson, Commentary: the materials project: a materials genome approach to accelerating materials innovation, APL Mater. 1 (2013), 011002, https://doi.org/10.1063/1.4812323.
[95] T.R. Koenig, Z. Rao, E. Chason, G.J. Tucker, G.B. Thompson, The microstructural and stress evolution in sputter deposited Ni thin films, Surf. Coat. Technol. 412 (2021), 126973, https://doi.org/10.1016/j.surfcoat.2021.126973.